# *New insights into the mechanism of iron transport through the bacterial Ftr-system present in pathogens*

Running title: Copper and iron-bound structure of FrtA-P19

Anne Soisig Steunou[1#], Armelle Vigouroux[1#], Magali Aumont-Nicaise[1], Stéphane Plancqueel[1], Alain Boussac[1], Soufian Ouchane[1], Solange Moréra[1*]

[1]Université Paris-Saclay, CEA, CNRS, Institute for Integrative Biology of the Cell (I2BC), 91198, Gif-sur-Yvette, France

# Equal contribution

* Corresponding author: solange.morera@i2bc.paris-saclay.fr; Tel +33 1 69 82 42 13 ORCID ID: 0000-0001-7781-0448/ anne-soisig.steunou@i2bc.paris-saclay.fr; Tel + 33 1 69 82 31 53 ORCID ID: 0000-0002-0731-0226

A. Vigouroux ORCID ID: 0000-0003-3531-5320; A. Boussac ORCID ID: 0000-0002-3441-3861; S. Ouchane ORCID ID: 0000-0002-8161-3866,

**Keywords**: Ftr-type transporter, ferrous iron transport, copper binding, iron oxidation, FtrA-P19

**Abbreviations**: *Rubrivivax gelatinosus*, Rg; EPR, electron paramagnetic resonance; WT, wild-type; RMSD, root mean square deviation; PDB, protein data bank; EDTA, ethylenediaminetetraacetic acid; ITC, isothermal titration microcalorimetry; DSC, Differential scanning calorimetry.

**Abstract**

Iron is an essential nutrient in bacteria. Its ferrous form, mostly present in low oxygen and acidic pH environments, can be imported using the specific Ftr-type transport system, which encompasses the conserved FtrABCD system found in pathogenic bacteria such as *Bordetella*, *Brucell*a and *Burkholderia*. The non-pathogenicity and versatile metabolism of *Rubrivivax gelatinosus* make it an ideal model to study the FtrABCD system. Here, we report a new aspect of its regulation and the role of the periplasmic proteins FtrA and FtrB using *in vivo* and *in vitro* approaches. We investigated the metal binding mode and redox state of copper and iron to FtrA by crystallography and biophysical methods. An 'as isolated' FtrA protein from the bacterial periplasm contained a copper ion ($Cu^{+}$) identified by electron paramagnetic resonance (EPR). Copper is coordinated by four conserved side chains (His and Met) in the primary metal site. Structural analysis of *R. gelatinosus* FtrA and FtrA homologues revealed that copper binding induces a rearrangement of the His95 imidazole ring, releasing thereafter space, as well as both Asp45 and Asp92 side chains, for iron binding in the secondary metal site. EPR highlighted that FtrA can oxidize the bound ferrous ion into the ferric form by reducing the bound $Cu^{2+}$ into $Cu^{+}$, both metal sites being separated by 7 Å. Finally, we showed that FtrB binds iron and not copper. These results provide new insights into the mechanism of ferrous iron utilization by the conserved FtrABCD iron transporter for which we propose a new functional model.

## Introduction

Bacteria have evolved various types of iron acquisition systems. In aerobic environments, iron is mostly found under its ferric form ($Fe^{3+}$) and imported by extracellular siderophores or iron-binding proteins produced by bacterial cells. The iron-loaded siderophores are internalized into the periplasm by a TonB-dependent transport system [1–3], and the ferric iron is imported into the cytoplasm by an ABC-type transporter such as the FbpABC system [4,5]. In low oxygen and acidic pH environments, iron is rather under its ferrous form ($Fe^{2+}$). Unlike the ferric iron, it is admitted that the ferrous iron is directly imported into the periplasm and uses different transport systems such as the ubiquitous FeoAB and the Ftr-type transporters [6].

The common element to all Ftr-type ferrous iron uptake systems is the conserved permease, named EfeU and FetM in *E. coli*, cFtr in *Campylobacter jejuni* and FtrC in *Bordetella*, *Brucella* and *Burkholderia* species [7–15]. This permease is also present in eukaryotes, namely Ftr1P in yeast, which is the only well characterized permease so far [16–18]. Besides this permease, the components of the Ftr systems vary depending on the studied organism. In *E. coli* O157:H7 strain and *Bacillus subtilis,* in addition to the EfeU permease, the EfeUOB system comprises two periplasmic proteins EfeO (cupredoxine-I type oxydase) and EfeB [19,20]. In *Bordetella*, *Brucella* and *Burkholderia spp*, the FtrABCD system consists of two periplasmic proteins FtrA and FtrB (putative cupredoxin-II type oxidase), a polyferredoxin FtrD and the permease FtrC [10,11,13]. In *Campylobacter jejuni* (Cj), the Ftr system includes only one periplasmic protein denoted P19 (FtrA homologue) equivalent to FetP in the uropathogenic *E. coli* strain F11 in addition to the permease [9,21]. In contrast to the well-known Ftr system in yeast where the multicopper ferroxidase Fet3p oxidizes the ferrous iron into ferric iron prior to its import through Ftr1P [22], no ferroxidase activity has been shown in the bacterial Ftr system yet. Instead, it has been proposed for the FrABCD system that the putative cupredoxin-II type oxidase FtrB [20] would oxidize $Fe^{2+}$ bound to FtrA into $Fe^{3+}$ [8,10].

The bacterium *Rubrivivax gelatinosus* from *Burkholderiales* family possesses the Ftr-type system encoding operon annotated *ftrAPBCD* (Fig. 1A and 1B) [23]. The periplasmic protein named here RgFtrA, shares around 60% sequence identity with both *Brucella melitensis* and *Bordetella pertussis*

FrtA and 50% sequence identity with CjP19 and EcFetP. Its non-pathogenicity and versatile energetic metabolism make this bacterium an interesting model for studying the FtrABCD transport system found in pathogenic bacteria. Moreover, *R. gelatinosus* has the ability to grow under different oxygen concentrations. In the presence of oxygen, this bacterium respires, whereas under anaerobic condition with light, it grows by anoxygenic photosynthesis [24]. In addition to the iron system FtrAPBCD, *R. gelatinosus* possesses an effective ferric transport system FbpABC [25] and in its genome, genes encoding the ferrous iron system FeoAB are also present. Expression of iron acquisition genes is usually regulated by the available iron in the medium: in the presence of iron, the transcriptional regulator Fur-$Fe^{2+}$ complex represses genes encoding different iron uptake systems such as those coding for the Ftr1P-type system [7,26], whereas under iron depletion, Fur is inactive and iron uptake genes are expressed. Oxygen concentration is another factor involved in the regulation of some ferrous iron transporters through the [4Fe-4S] cluster of the transcriptional regulator FNR. It was shown that under low oxygen concentration, FNR activates the expression of *feo* genes in *E. coli* and *Shigella flexneri* [27,28].

In this work, we focused on the two periplasmic proteins FtrA and FtrB from the *R. gelatinosus* FtrAPBCD system. We provide evidence showing the regulation of *ftrAPBCD* operon by iron and by oxygen *via* FNR global regulator. We investigated the structural and biochemical properties of RgFtrA towards both copper and iron metal sites, their redox state and their binding mode. Structural comparison of high-resolution RgFtrA structures (apo, copper as well as copper and iron forms) revealed a key histidine residue, strictly conserved, which explains the sequential binding of Cu then Fe as first suggested for CjP19 [29]. We demonstrate that RgFrtA has a ferrous iron oxydase activity and that the putative cupredoxin-II type oxidase RgFrtB binds iron and not copper as a starting point for further investigations of its putative role in $Fe^{3+}$ transport. Overall, our data revisit a previous proposed model by providing new insights into the mode of function of the conserved FtrABCD transporters.

## Results

***ftrAPBCD* operon and its regulation.** The *ftr* operon (*ftrAPBCD*) of *R. gelatinosus* (Fig. 1B) is quite similar to that of *Brucella, Bordetella* and *Burkholderia* species except the presence of an additional gene encoding the outer membrane porin FtrP [10,11]. Analyses of the promoter sequence of *ftrA* gene with PRODORIC database (https://www.prodoric.de/vfp/) [30] revealed, in addition to the presence of a Fur box, an FNR binding site located upstream of the Fur box, suggesting that the expression of the *ftrAPBCD* operon could be under the dual transcriptional control by the iron-sensing Fur and the oxygen-sensing FNR regulators. To verify this hypothesis, we analyzed the transcription of *ftrAPBCD* genes of the wild-type (WT) and the Δ*fnr* mutant, lacking FNR regulator, by semi-quantitative RT-PCR under three oxygen conditions (aerobic (AE), microaerobic (MA) and anaerobic photosynthesis (PS) conditions), in malate medium with iron or in iron-depleted malate medium. First, because the cDNA was synthetized using an *ftrD* reverse primer, this experiment confirmed that *ftrAPBCD* is an operon, since using this *ftrD*-amplified cDNA, we were able to amplify the distal gene *ftrA* (Fig. 1B-C). On the other hand, the RT-PCR data clearly showed that expression of the *ftrAPBCD* operon was induced under iron deficiency conditions. Moreover, it also showed that the expression of *ftrAPBCD* operon was oxygen dependent. Indeed, under iron depleted conditions, in the WT, expression of *ftrA* and *ftrD* genes was higher under microaerobic and anaerobic conditions than under aerobic condition (Fig. 1C) strongly suggesting a regulation by FNR. This hypothesis was validated by analyzing *ftrAPBCD* expression in the Δ*fnr* mutant background. Δ*fnr* mutant does not grow under strict photosynthesis conditions, we therefore compared the *ftrAPBCD* expression profile under aerobic *versus* microaerobic conditions. As shown in Figure 1C, expression of *ftrAPBCD* in the Δ*fnr* mutant was no longer induced under microaerobic condition, in sharp contrast to the WT. In the WT, FtrA was more abundant under iron depleted condition as expected, while in Δ*fnr* mutant, the abundance of FtrA was drastically reduced (data not shown). The expression level depends both on iron availability, very likely *via* Fur and on oxygen concentration *via* FNR regulator.

**RgFrtA is involved in iron transport.** For a previous study on iron import and resistance to heavy metals, we have constructed the Δ*ftrATp* and *fpbAKm* single defective mutants as well as the *fbpAKm*-Δ*ftrATp* (*ffA*) double mutant. *fbpA* codes for the periplasmic iron binding protein of the ferric iron ABC transporter FbpABC system [25]. In the malate medium containing iron, the same growth was observed for all strains under microaerobic condition regardless of the medium pH (Fig. S1A and S1B). In contrast, in iron depleted malate medium at pH 6 under microaerobic condition (Fig. 2), the Δ*ftrATp* mutant grew with two phases: a lag phase of 18 hours before regaining a growth rate similar to the WT whereas the *fpbAKm* mutant grew quite similarly to the WT. At pH 7, no phenotype was observed for Δ*ftrATp* mutant and *fpbAKm* growth was slowed down and did not grow as well as the WT.

The most important growth inhibition was observed with the double mutant *ffA* at both pHs revealing that Ftr and Fbp are active and complementary. Moreover, no other iron transporter seems to compensate the absence of both Ftr and Fbp systems, suggesting that in our tested conditions, the ubiquitous *feoAB* system was not functional. To verify it, we constructed and observed the phenotype of the *feoBKm* single mutant and the *feoKm*-Δ*fbpATp (ffO)* double mutant (Fig. S1). Because *feoBKm* behaved as the WT and *ffO* showed a phenotype similar to *fpbAKm*, the Feo system seems non-functional in *R. gelatinosus*.

**Structures of apo His-tag RgFtrA and RgFtrA, and comparison with apo structures of homologues.** To obtain the soluble FtrA of *R. gelatinosus* in *E. coli* cytoplasm, the *ftrA* gene was synthetized without the signal sequence encoding the first 23 amino acids, which serve for the translocation to the bacterial periplasm. An *ftrA* gene coding for the His-tag RgFtrA protein was also synthetized with no signal peptide and with additional 11 amino acids including 6 histidine residues at the C-terminus. Both proteins (RgFtrA and His-tag RgFtrA) were purified from the cytoplasm of *E. coli* as a dimer in solution, according to gel filtration measurements. The numbering used for the description of residues corresponds to the mature protein of 162 amino acids (without the signal peptide) in order to simplify its comparison with the well studied P19 homologue from *C. jejuni* [9,29].

Using thermal denaturation experiments by differential scanning calorimetry (DSC), adding 0.5 mM or 1 mM ethylenediaminetetraacetic acid (EDTA, a strong chelating agent) to RgFtrA and His-tag RgFtrA had no effect on the *Tm* of 52.1 °C and 53.7 °C, respectively (Fig. S2), indicating that both proteins were in an apo form, confirmed by X-ray fluorescence scans on RgFtrA crystals at synchrotron beamline. They both crystallized under the same conditions leading to isomorphous crystals diffracting at 1.4 Å and 1.23 Å, respectively, and containing a very similar homodimer in their asymmetric unit with an average root mean square deviation (RMSD) of 0.12 Å for 312 Cα atoms (Fig. 3A, Tables 1 and 2). A full RgFtrA monomer was built in the electron density maps, while for the three other monomers (RgFtrA and His-tag RgFtrA), between 154 and 157 amino acids were built because their C-terminus including the His-tag was not visible. FtrA forms a recognizable dimer like a prolate spheroid with an interface of 1863 $Å^2$ per subunit corresponding to an average of 20.5% of the total surface area of each monomer and 50 amino acids per monomer involved in 18 hydrogen bonds and 6 salt bridges. The dimeric interface, which encompasses two β sheets (β6 and β9) and 5 loops, is characteristic of biological interactions [31].

RgFtrA resembles the *C. jejuni* P19 (CjP19; [9,29]) and the uropathogenic *E. coli* strain F11 FetP [32]. Indeed, SSM-EBI (http://www.ebi.ac.uk/msd-srv/ssm) reports RMSD of 0.85-1.13 Å between RgFtrA and the numerous structures of CjP19 over 146-148 Cα atoms with 55% sequence identity, and RMSD of 0.91-1.13 Å with the structures of FetP over 146-147 residues with 52% sequence identity. The structures of RgFtrA and His-tag RgFtrA confirmed the absence of any metal. Instead, a water molecule is located in the primary metal binding site about 1.3 Å from the expected copper position represented by a Zn ion modelled at 10% occupancy in CjP19 having led the authors to describe this Zn-CjP19 structure as an apo form (PDB 3LZN). The water molecule makes hydrogen bonds with the side chains of three conserved residues: His41 (His42/His44 in CjP19/FetP), Glu43 (Glu44/Glu46 in CjP19/FetP and His131 (His132/His127 in CjP19/FetP) (Fig. 3A). Remarkably, comparison of the apo structures of RgFtrA, CjP19 (PDB 3LZN) and EcFetP (PDB 3NRQ) revealed a major local difference concerning the conserved copper ligand, His95. Indeed, in RgFtrA only, the imidazole ring of His95 is rotated by about

60° placing the NE2 atom 4.4 Å away from the copper binding site (Fig. 3B). In this position, His95 interacts with the side chains of Asp45 and Asp92 (Fig. 3B).

**The primary site of RgFtrA displays a strong preference for copper binding *in vitro***. Using thermal denaturation experiments by DSC, the primary metal site was investigated on the RgFtrA (30 μM) treated with EDTA to remove any metal traces (Table 3 and Fig. S3). DCS analyses revealed that $Fe^{2+}$, $Fe^{3+}$, and $Mg^{2+}$ did not alter the *Tm* whereas $Mn^{2+}$ has a modest effect. Significant increase of the *Tm* by ~6-7°C was observed with $Co^{2+}$ and $Zn^{2+}$, by ~10°C with $Cd^{2+}$ and by ~20°C with $Ni^{2+}$. Drastic shifts > 23°C, were observed for $Cu^{+}$ and $Cu^{2+}$. The same approach by nano-differential scanning fluorimetry (nanoDSF) on Tycho NT.6 instrument led to similar results as DSC (Fig. S4). Performing these experiments with the reductant agent Tris(2-carboxyethyl)phosphine (TCEP) added to ferrous iron gave the same result as ferrous iron alone without TCEP (data not shown).

Binding of $Cu^{2+}$, $Ni^{2+}$ and $Zn^{2+}$ to the RgFtrA treated with EDTA was further explored using ITC (Fig. 4). As expected, the best affinity was measured with $Cu^{2+}$ with a $K_D$ value of 0.6 μM. Microcalorimetry data confirmed the 1:1 binding stoichiometry revealing a negative enthalpy change.

**The secondary metal binding site of RgFtrA binds iron *in vitro.*** We explored the second metal binding site by DSC using the RgFtrA treated with EDTA and loaded with equimolar $CuCl_2$ at acidic (6.5) and basic (8) pH values (Table 3 and Fig. S5). DCS analyses clearly revealed that RgFtrA-Cu has a strong preference for iron with large *Tm* shifts of ~15°C at pH 6.5 (Table 3). $Mn^{2+}$ has a modest effect and no shift was observed with $Mg^{2+}$ or $Co^{2+}$. Similar results were obtained at pH 8 with *Tm* shifts less pronounced (Fig. S5). NanoDSF on Tycho NT.6 instrument confirmed DSC analyses (Fig. S6).

Binding of $Fe^{2+}$ to the RgFtrA treated with EDTA and loaded with equimolar $CuCl_2$ was further explored using ITC at pH 6.5 and 8 (Fig. 5). The similar measured $K_D$ values of 3.3 and 5.8 μM indicated that pH has not real effect on iron binding. The microcalorimetry data confirmed the 1:1 binding stoichiometry and revealed a negative enthalpy change.

**Primary metal binding site**

**$Cu^{+}$ bound.** A Strep-tag RgFtrA protein was synthetized with a strep tag of 8 amino acids at the C-terminus (the signal peptide was conserved). The strep-tag *ftrA* synthetized gene under its own regulated promoter was cloned in a replicative plasmid pBBR1-MCS2 and expressed in the Δ*ftrATp* mutant. The 'as-isolated' Strep-tag RgFtrA was expressed and purified from the periplasm of *R. gelatinosu*s to determine the presence of a physiologic metal if any and its redox state. The first batch of purified protein crystallized in conditions different from those used for the His-tag RgFtrA and RgFrtA expressed in the cytoplasm of *E. coli* (Tables 1 and 2). DSC experiments showed that the first batch of 'as-isolated' Strep-tag RgFtrA was already loaded with metal because addition of EDTA resulted in a significant decrease of the *Tm* by ~9°C to reach a value closer to that observed for the apo His-tag RgFtrA (Fig. 6A). In addition, an X-ray fluorescence spectrum on crystals measured at synchrotron beamline detected only one type of metal identified as being copper. Therefore, a SAD dataset was collected at the copper anomalous signal peak at 1.3 Å resolution (Table 1). The electron density maps revealed the presence of two very well defined copper ions located at the oligomeric interface (one copper per subunit, Fig. 3C). Their low temperature factors (*B*-factor) of 11.8/11.2 $Å^2$ in chain A/chain B imply full occupancy. Their coordination is tetrahedral with distances of 2.02-2.37 Å with the conserved protein side chains of His41, Met88, His95 and His131' from the neighbouring subunit (Table 4). The EPR spectrum recorded on the same batch of protein showed no detectable metal signal (Fig. 6B). In contrast, upon addition of an HCl drop (~ 18%), a $Cu^{2+}$ signal was detected (Fig. 6B), demonstrating that the 'as-isolated' protein used for this study binds copper in its $Cu^{+}$ redox state. However, more batches of 'as-isolated' Strep-tag RgFtrA were prepared and EPR on these different batches showed that the Strep-tag RgFtrA could be isolated with trace of $Cu^{2+}$ (not shown). Superposition of the structures of Strep-tag RgFtrA-$Cu^{+}$ and apo RgFtrA showed that in the apo RgFtrA, the water molecule in the primary metal binding site is at 1.8 Å from the bound $Cu^{+}$ ion in the Strep-tag RgFtrA-$Cu^{+}$, near the His95 side chain, which interacts with the $Cu^{+}$ ion (Fig. 3D). The position of this water molecule was possible because His95 side chain was out of the copper site as described above in the paragraph of the apo structures.

**$Cu^{2+}$ bound.** RgFtrA (expressed and purified from the cytoplasm of *E. coli*) loaded with equimolar $CuCl_2$ and 1 mM $FeSO_4$ crystallized in conditions containing at least 50 mM $MgCl_2$ (Table 2). Removing $MgCl_2$ prevented crystals growth. Two crystals denoted X1 and X2 grown with 100 and 50 mM $MgCl_2$,

respectively, were collected. X-ray fluorescence spectrum measured from the crystals did not indicate the presence of iron and data collected at the iron anomalous signal peak lacked anomalous signal. A full occupancy $Cu^{2+}$ was modelled in each subunit in both structures taking into account that the protein was co-crystallized with $CuCl_2$. The $Cu^{2+}$ occupies the primary metal site as expected making the same protein contacts compared with the reducing copper form (Table 4).

**$Ni^{2+}$ bound**. Because nickel ions have a stability effect on RgFtrA as strong as copper ions as shown by DSC, we investigated their binding mode. In the presence of 20 mM $NiSO_4$, the His-tag RgFtrA crystallized in the same conditions as the apo His-tag RgFtrA and RgFtrA leading to isomorphous crystals (Table 2). The presence of nickel in the crystals was confirmed by X-ray fluorescence and data were collected at the nickel anomalous edge. The electron density maps revealed the presence of nickel in the primary metal site of only one subunit despite a protein:nickel ratio of 1:200. The side chain of His95 takes two alternative positions with similar occupancies, one with the imidazole ring bound to the metal, the other pointing away from it as observed in the apo form (Fig. 7A). The $Ni^{2+}$ was thus refined with the assumed 50% metal occupancy resulting in a B-factor of 33.8 Å². It interacts with His41, His95 and His131' from the neighbouring subunit and makes a very short contact with His95 (Fig. 7A and Table 4). The $Ni^{2+}$, which is 0.6 Å from the $Cu^{+}$ ion is close to Glu43 carboxylate and far away from Met88 (Fig. 7B and Table 4). The other subunit of the His-tag RgFtrA-Ni complex contains a water molecule as observed in the apo form (Fig. 7C).

## Secondary metal binding site

**$Fe^{3+}$ bound.** Crystals of 'as-isolated' Strep-tag RgFtrA ($Cu^{+}$ bound) purified from the periplasm of *R. gelatinosu*s were soaked with 0.1 M $FeCl_3$. Crystals turned orange suggesting ferric ion incorporation. An X-ray fluorescence spectrum measured from the crystal detected the presence of iron. A SAD dataset was collected at the iron anomalous signal peak at 2.75 Å resolution (Table 1). The asymmetric unit contains one dimer and each subunit binds an iron ion in the secondary metal site adjacent to the copper site located at the protein surface (Fig. 8A and 8B). $Fe^{3+}$ was modelled taking into account that the crystal was coloured before X-ray exposure. Each $Fe^{3+}$ binds to the Glu2, Glu43 and Asp92 carboxylates

(Fe-O distances ranging from 1.7 to 2.3 Å) showing the shortest interaction with Asp92 (Table 5 and Fig. 8A). The two metal ions ($Cu^{+}$ and $Fe^{3+}$) are separated by ~ 7 Å (Fig. 8C).

**$Mg^{2+}$ bound.** Co-crystallization with 4 mM $FeSO_4$ of the 'as-isolated' Strep-tag RgFtrA ($Cu^{+}$ bound) purified from the periplasm of *R. gelatinosu*s led to crystals different from those obtained with the protein without $FeSO_4$ likely due to the presence of a very high concentration of 200 mM $MgCl_2$ in the crystallization conditions (Table 1). The asymmetric unit contains three very similar dimers, each subunit showing full occupancy of the primary metal site with essentially the same protein-$Cu^{+}$ interactions (Table 4). A magnesium ion was modelled in all secondary metal site subunits being ~ 7 Å apart from the $Cu^{+}$ ion (Table 5 and Fig. 8D). Chains A, B and F show an octahedral coordination with Glu43, Asp92 and four water molecules at distances of 1.92-2.4 Å compatible with a full ion occupancy (Table 5 and Fig. 8D). The Glu2 carboxylate occupies a different position in the magnesium-ligated complex *versus* the iron-ligated complex, where it makes water-mediated magnesium interactions instead of direct metal interaction (Fig. 8E). In the structures of RgFrtA denoted X1 and X2 (Table 2) obtained from crystallization conditions with much lower concentration of $MgCl_2$ (100 and 50 mM, respectively), the electron density maps suggest the presence of a $Mg^{2+}$ in each secondary metal site due to a short contact with Asp92 side chain (Table 5). Each $Mg^{2+}$ ion seems well coordinated in both X1 and X2 structures compared with those in the structure obtained with 200 mM $MgCl_2$.

**The bound-copper RgFtrA can oxidize the ferrous iron into ferric iron.** The “as purified” RgFtrA treated with EDTA or not exhibited the EPR spectrum shown in Fig. 9 (black spectrum) indicating that the protein was devoid of EPR detectable metals. Upon reconstitution with $Cu^{2+}$ (equimolar), the protein exhibited a $Cu^{2+}$ EPR spectrum (red spectrum). Then, $Fe^{2+}$ was added in a stoichiometric amount directly in the EPR tube. Similar results were obtained with either $FeCl_2$ or $FeSO_4$ (not shown). After this $Fe^{2+}$ addition, the $Cu^{2+}$ EPR signal decreased significantly and a spin $S = 5/2$ $Fe^{3+}$ EPR signal between ~600 gauss and ~2000 gauss appeared (blue spectrum). This experiment showed that the bound $Cu^{2+}$ has a redox potential high enough for oxidizing the $Fe^{2+}$ into $Fe^{3+}$. After further addition of $Fe^{2+}$ to reach a concentration twice that of the protein, the amplitude of the $Fe^{3+}$ and $Cu^{2+}$ signals remained unchanged

(green spectrum) showing that there was no detectable auto oxidation of the $Fe^{2+}$ in these conditions. Moreover, this suggests that this was not the $Fe^{2+}$ present in the bulk, which was responsible for the $Cu^{2+}$ reduction bound to the protein. The copper reduction more likely occurs after the binding of $Fe^{2+}$ in its site. The distance of 7 Å between the cooper and iron binding sites given by the crystal structures is perfectly compatible with such an electron transfer, see for example [33]. With a redox potential similar for the $Cu^{2+}/Cu^{+}$ and the $Fe^{3+}/Fe^{2+}$ couples, and assuming that both the copper binding site and iron binding site are fully occupied in the EPR conditions, we would expect a two-fold decrease of the amplitude of the $Cu^{2+}$ signal. The remaining $Cu^{2+}$ signal amplitude was in fact closer to 30 % of the signal prior to $Fe^{2+}$ addition. The binding to the protein increases the $E_m$ of the $Cu^{2+}/Cu^{+}$ couple and decreases the $E_m$ of the $Fe^{3+}/Fe^{2+}$ couple when compared to the $E_m$ of these metals in solution so that the $E_m$ of the $Cu^{2+}/Cu^{+}$ couple becomes slightly above that of the $Fe^{3+}/Fe^{2+}$ couple.

**The putative cupredoxin-II type oxidase FtrB binds iron and not copper.** To investigate the role of RgFtrB, the single defective mutant Δ*ftrBTp* and the double defective mutant *fbpAKm*Δ*ftrBTp (ffB)* were constructed. Growth assays with Δ*ftrBTp* showed exactly the same phenotype as Δ*ftrATp* demonstrating that FrtB and FrtA share a common role in iron transport (Fig. S1). Using the mature RgFtrB (30 μM) expressed and purified from *E. coli* cytoplasm and treated with EDTA to remove any metal traces, DSC analyses revealed that the presence of $Cu^{2+}$ did not alter the *Tm* in contrast to $Fe^{2+}$ (and $Fe^{3+}$) which drastically impacted the *Tm* by ~ 24.3°C (Fig. 10). The nano-differential scanning fluorimetry (nanoDSF) could not be performed due to the lack of tryptophan in RgFtrB. We showed that FtrB could bind iron and no copper.

## Discussion

### Regulation of iron transporter genes

Bacteria respond to iron-limiting conditions by inducing the expression of proteins involved in iron acquisition to capture and import the sparsely iron present in their environment. The activation of iron transporters relies on the availability of iron and its redox state and thus also on the oxygen concentration. In this work, we show that transcriptional regulator FNR (sensitive to oxygen) regulates the *ftrAPBCD* genes of *R. gelatinosus* and very likely in other bacteria. Indeed, we have identified an FNR binding site upstream of the Fur box in the promoter region of genes encoding a Ftr1P system in all analyzed bacteria including *E. coli*, *C. jejuni*, *B. pertussis, P. syringae*, *P. palustris* or *B. subtilis* (Fig. 11). It should be noted that in *B. abortus* (Fig. 11), which lacks Fur, the FNR binding site overlaps the binding site denoted ICE of the iron response transcriptional regulator Irr, involved in the regulation of the FtrABCD operon [11]. Overall, this strongly suggests that *ftr1P* operon expression could be under the dual transcriptional control by the iron-sensing Fur or Irr and the oxygen-sensing FNR regulators.

*R. gelatinosus* possesses three iron transporter systems in its genome, the Fbp, Feo and Ftr systems. The FbpABC systems are known to transport ferric iron while the FeoAB and Ftr1P systems bind ferrous iron. Our growth analyses in iron-depleted media, at acidic and neutral pH suggested that the Ftr iron transporter is required at acidic pH and microaerobic condition. This result is in agreement with the function of each transporter ($Fe^{2+}$ for Ftr and $Fe^{3+}$ for Fpb) because acidic pH and low oxygen favor the ferrous iron form.

FNR is known to activate the transcription of the ubiquitous iron transporter FeoABC [27]. A *feoAB* operon is present in *R. gelatinosus*, nonetheless, the growth inhibition phenotype of the double mutant *ffA* suggested that the Feo system is not active. It should be noted that in other bacteria possessing the FtrABCD system, no functional Feo system has been identified so far. This is the case for *Bordetella*, *Brucella* and for many *Burkholderia* [10,11,14].

### A conserved histidine orchestrates the sequential metal binding order in FtrA

This work reveals the structural basis of FtrA displaying two conserved metal binding sites referred as primary and secondary metal sites for all orthologues. FtrA/P19 proteins are all dimeric and the two

adjacent binding metal sites are formed at the interface between the two monomers. When present, the physiological metal ion bound to the primary metal site is copper as demonstrated by EPR experiments on the 'as isolated' Strep-tag RgFtrA purified from the periplasm of *R. gelatinosus*. Therefore, the purified 'as isolated' Strep-tag RgFtrA could remain loaded with endogenous reduced $Cu^{+}$ ion although the overall purification process was done under aerobic conditions. This indicates that the four copper-coordinating amino acids (His41, Met88, His95, His131) forming a typical tetrahedral geometry have a remarkable ability to stabilize $Cu^{+}$ and protect it from natural oxidation. Of particular note is that while the copper ion is not required for RgFtrA stability and folding (as demonstrated by the purified apo form and crystal structures), DSC, nanoDSF and affinity measurement all showed copper as the best ligand of the primary metal site, in agreement with the physiological metal.

A remarkable outcome of this work is demonstrating that the primary metal site is not preformed. Our apo form versus copper-ligated structures clearly revealed the important role of the side chain of His95. Indeed, its imidazole ring plays a regulatory role in the sequential order of metal binding. In the absence of any metal, His95 interacts with both carboxylates of Asp45 and Asp92, which both form the secondary metal site. Copper binding induces a rotation of His95 side chain, which seals the primary metal binding site, by interacting tightly with the copper ion thus leaving the space for iron to bind to the secondary metal site. The ferrous iron interacts directly with the side chains of Glu2, Glu43 and Asp92 and through water molecules with Asp45. Glu43 is ~ 4 Å distant from the copper and thus makes no direct interaction with this metal (Table 4). No obvious conformational change was observed for Glu43 in our eight-crystal structures (apo form *versus* metal complexes), however only a slight displacement could bring its side chain closer to copper site as observed in CjP19 structures [29]. The structure-based sequence alignment of RgFtrA with homologues such as CjP19 (PDB 3LZN) and EcFetP (PDB 3NRP) indicates that all residues involved in metal binding are conserved (Fig. 12A). Copper coordination occurs through His41/His42/H44, His95/His95/His97, His131/His132/H127 and Met88/Met88/Met90 in RgFtrA/CjP19/EcFetP and iron coordination via 3 side chains (Glu2/Glu3/Glu4, Glu43/Glu44/Glu46 and Asp92/Asp92/Asp94). The structures of RgFtrA and CjP19 (PDB 1I0V) in complex with Cu and Fe in oxidizing condition superimpose with a RMSD of 0.8 Å for all Cα atoms.

Their copper and iron bind at the same position with the protein side chains around each metal overlapping and making similar metal contacts (Fig. 12B). Overall, our structures point out that the apo structure of CjP19 (PDB 3LZN) should maybe be reconsidered as not an apo structure.

The structure of RgFtrA-$Cu^{+}Ni^{2+}$ revealed that the nickel binds only the three His of the four side chains of the primary binding site, suggesting that Met88 is specific for copper binding and positioning, in line with the results of the corresponding variant M88I on CjP19 (Chan et al 2020). Although DSC and nanoDSF showed that $Mg^{2+}$ is not a ligand of RgFtrA, excess of $MgCl_2$ in the crystallization conditions lead to $Mg^{2+}$ bound in the iron binding site. Thus, $Mg^{2+}$ such as $Mn^{2+}$ act as iron mimics. The metal coordination by Glu2/Glu3 observed in iron-bound structures of RgFtrA and CjP19, respectively, was not observed in the $Mn^{2+}$-CjP19 (PDBs 3LZR and ELZQ) and our $Mg^{2+}$-RgFtrA structures. This emphasizes the previous assumption that Glu2/Glu3 participates to iron selectivity and has an important role. DSC and nanoDSF confimed iron as the preferred metal in agreement with the physiological ligand of the secondary metal site of FrtA-P19.

**FtrABCD iron transport system**

The four-component Ftr system FtrABCD is highly conserved among *Brucella, Bortedella* and *Burkholderia* gathering different species including *R. gelatinosus* [10,11,14,15] and suggesting similar functional mode for these iron transporters. Until now, no or few biochemical data is available on the four proteins of this Ftr system. As mentioned in the introduction, the best-characterized Ftr system is from yeast, composed of the permease Ftr1p and the multicopper ferroxidase Fet3p. Fet3p captures $Fe^{2+}$ by conserved acidic residues and oxidizes it by a $Cu^{2+}$ in Type-1 site defined by conserved HisHisCys residues, resulting in $Fe^{3+}$ production. Fet3p interacts with Frt1p and the iron oxidation occurs concomitantly to the transport of ferric iron [22]. The yeast Ftr model for the bacterial Ftr systems used as a reference and has not yet been validated in bacteria due to the lack of data on iron oxidation. Here for the first time, we have experimentally identified FtrA as a protein with ferrous iron oxydase activity able to oxidize the ferrous ion into ferric iron in a Cu dependent manner. Therefore, although FtrA contains only one atypical copper site (not a Type-1 site) and has no resemblance with Fet3p, FtrA seems to play a similar function as Fet3p. Glu43/Glu44 in RgFtrA/CjP19 located between the copper and iron

sites as described above has been proposed to facilitate electron transfer between the two metals [29]. For the bacterial two-component Ftr systems with P19/FetP and cFtr/fetM in *C. jejuni*/*E. coli*, based on structural data, we predict that CjP19 and EcFetP would also display a ferrous iron oxydase activity similar to FtrA.

FtrB until now was considered as a new cupredoxin based on sequence alignment, conservation of several amino acids and structural model analyses. Nonetheless, as highlighted recently [15], no biochemical analyses have so far confirmed copper binding in FtrB. Instead, FtrB has been suggested as a protein with a key function in copper-dependent iron oxidation and a model was proposed in which FtrA delivers $Fe^{2+}$ to FtrB, which will then oxidize the iron and transfer it to the FtrC permease [8,10]. We have shown that RgFrtB does not bind copper but iron likely through conserved acidic residues at positions 42, 44, 51 and 76. Carboxylate at position 77 in *R. gelatinosus* is also conserved being a Glu in *R. gelatinosus* and an Asp in *Brucella* and *Bortedella* FtrB homologues based on multiple-sequence alignment (Fig. 13A). AlphaFold2 prediction model (ColaFold on google) showed that the conserved acidic residues are surface-exposed and could form an iron binding site (Fig. 13B). The FtrB protein, which plays an important role in the Ftr system, since Δ*ftrBTp* and Δ*ftrATp* mutants share the same phenotype, is very likely not a cupredoxin. We suggest an iron ($Fe^{3+}$) chaperon activity for FtrB.

In the two-component Ftr systems with P19/FetP (FtrA homologues) and cFtr/fetM in *C. jejuni*/*E .coli*, no cupredoxin has been identified yet. However, a large extra-periplasmic domain is present in FtrC from *C. jejuni* and *E. coli* and seems to interact with P19/FetP [29]. Based on these observations, we propose an alternative model to the one proposed in *Bordetella* where, first, FtrA is a Cu-dependent ferrous iron oxydase which oxidizes the $Fe^{2+}$ to $Fe^{3+}$ (Fig. 14) and then the oxidized iron is transferred to the permease FtrC through the iron chaperon FtrB. The reduced $Cu^{+}$ in FtrA could be regenerated by transferring the harvested electrons to the polyferredoxin FtrD predicted to act as an electron sink, allowing the recycling of electrons from $Cu^{+}$ to $Cu^{2+}$ of FtrA. [8,10,11,14].

**Conclusion**

Our work brings new insights into the functional mode of the highly conserved bacterial four-component FtrABCD ferrous iron transport system through the study of FrtA and FtrB proteins. We highlighted a role of FrtA as a ferrous iron oxidase and FrtB as an iron chaperone, likely linking FtrA and FrtC. Our model functionally resembles the yeast Ftr system composed of Frt1p-Fet3p. Our structural data showed that the side chain of His95 in FtrA guides the sequential order of metal binding where the primary copper site must be filled first before the iron site. The copper metal ligand of FtrA is thus essential for iron binding and oxidation. More biochemical data are required to validate our new Ftr-system model such as protein interactions.

## Materials and methods

**Bacterial strains and growth.** *R. gelatinosus* was grown at 30°C, in the dark either in aerobically (high oxygenation: 20 ml medium in 250 ml flasks), or microaerobically (low oxygenation: 50 ml medium in 50 ml flasks) conditions or with light under anaerobic conditions (filled tubes) in malate or in malate iron depleted growth medium. *E. coli* was grown overnight at 37°C in LB medium. Antibiotics (50 µg/ml) such as ampicillin, kanamycin (Km), trimethoprim (Tp), were added when appropriate. One liter of malate medium consists of: 30 ml 100g.l$^{-1}$ malate $NH_4$, 20 ml of concentrate base (34 mM EDTA, 130 mM KOH, 58 mM $MgSO_4$, 22 mM $CaCl_2$, 7.5 µM $(NH_4)6Mo7O_{24}$, 0.4 mM nicotinic acid, 74 µM thiamine, 2 µM Biotin, 356 µM $FeSO_4$), 20 ml 1M phosphate buffer pH 7, 1g N-Z amine (Merck ; Ref :C7290), 1 ml of metals (0.85 mM EDTA, 0.28 mM $ZnSO_4$, 9.1 mM $MnSO_4$, 1.5 mM $CuSO_4$, 0.85 mM $Co(NO_3)$, 0.46 mM $Na_2B_4O_7$, 18 mM $FeSO_4$) and 1g of yeast extract.

Bacterial strains and plasmids are listed in Table S1. Growth under microaerobic conditions of *R. gelatinosus* strains was measured at $OD_{680nm}$ during 40 h using the Tecan Infinite M200 luminometer (Mannerdorf, Switzerland). For the photosynthetic growth, strains were grown with light in filled well plates cover by a sealed membrane.

**Gene cloning, plasmid constructions and mutant strains construction.** Standard methods were performed according to Sambrook et al. [34]. Primers used are listed in Table S2. To delete *ftrB* gene, two PCR fragments obtained with RG479-RG480KpnI and RG481KpnI-RG482 primers were digested by KpnI and cloned in pGemT-easy leading to pGe-Δ*ftrB*. Then the Tp cartridge was inserted at the KpnI site within Δ*ftrB* of pGe-Δ*ftrB*. The integrative plasmid pGe-Δ*ftrBTp* was used to inactivate *ftrB* by electroporation in the WT and in the mutant *fbpAKm* in order to construct the single mutant Δ*ftrBTp* and the double mutant *ffB* (*fbpAKm*-Δ*ftrBTp*) of *R. gelatinosus*. KS-*feoBKm* was obtained from DNA isolated from *copA::Ω-feoB::Tn5* (unpublished data) digested by PstI and cloned into Bluescript KS+. Insertion of the transposon in *feoB* in the *copA::Ω* mutant [35] makes the strain more resistant to copper than the single mutant *copA::Ω* (unpublished data). This plasmid was used to inactivate *feoB* by electroporation in the WT. To construct KS-*fbpA*Tp, we replaced the Km cartridge of KS-*fbpA*Km by the Tp cartridge by digesting the plasmid and p34S-TP with SmaI.

We ligated them and obtained KS-*fbpA*Tp. This plasmid was used to transform the *feoBKm* mutant to get the *feoBKm-fbpATp* (*ffO*) double mutant. Transformants were selected on malate plates supplemented with the appropriate antibiotics under aerobic conditions. Genomic DNA was prepared from the ampicillin sensitive transformants and confirmation of the presence of the antibiotic resistance marker at the desired locus was performed by PCR.

**mRNA preparation and qPCR.** Total RNA was purified from WT and FNR$^-$ mutant cells grown under different oxygenic conditions (aerobic (AE), microaerobic (MA) and photosynthesis (PS) conditions) in malate medium (M) composed of malate NH4, phosphate potassium buffer at pH 7, iron, vitamin free casamino acids, metal 44 and yeast extract or in an iron depleted malate medium (-Fe) as described in [36]. For semi-quantitative qPCR, cDNA were generated from 1 µg of total RNA with a specific reverse primer RG498 using the Superscript IV (Invitrogen) and by following the manufacturer's protocol. PCR was done with 2 µl of cDNA with specific primers (table SII) to amplify fragments of *ftrA* (RG489-RG490) and *ftrD* (RG497-RG498) genes. Amplified products were analysed on a 1.4% agarose gel.

**Cloning, expression and purification of mature recombinant His-tag RgFtrA.** The synthetic gene (Genscript) coding for RgFtrA without its signal peptide and fused to 11 amino-acids including a C-terminal His-tag was inserted into pET-26b. *E. coli* BL21 pLysS were transformed by pET26b-*ftrAH*$_6$. Cells were grown at 37°C in LB broth supplemented with 1 mM isopropyl β-D-1-thiogalactopyranoside to induce protein production. Cells were centrifuged, resuspended in a buffer of 50 mM Tris-HCl, pH 8, 20 mM imidazole and 300 mM NaCl, and disrupted by sonication. After centrifugation at 25,000 g for 30 min at 4°C, the supernatant was loaded onto a 5 ml His-Trap HP column (GE Healthcare). Protein elution was performed with 50 mM Tris-HCl pH 8, 300 mM imidazole and 300 mM NaCl. Protein fractions were loaded onto a gel filtration column (HiLoad 26/60 Superdex 200 prep grade, GE Healthcare) equilibrated with 50 mM Tris-HCl pH 8 and 150 mM NaCl. The protein fractions were pooled, concentrated and stored at -80°C. This protein led to the first structure of apo His-tag RgFtrA at 1.4 Å resolution.

**Cloning, expression and purification of mature recombinant RgFtrA and RgFtrB.** The synthetic gene (Genscript) coding for the mature RgFtrA (without the signal peptide) was inserted into pET-26b.

The synthetic gene (Genscript) coding for the mature RgFtrB was inserted into pET-29b. *E. coli* BL21 pLysS were transformed by pET26b-*ftrA* or pET29b-*ftrB*. Cells were grown at 37°C in LB broth supplemented with 1 mM isopropyl β-D-1-thiogalactopyranoside to induce protein production. Cells were centrifuged, resuspended in a buffer of 50 mM sodium acetate, pH 4.5 and disrupted by sonication. After centrifugation at 25,000 g for 30 min at 4°C, the supernatant was loaded onto a cation-exchange chromatography (HiTrap SP 5ml, GE Healthcare). Protein elution was performed with a linear gradient of 0-1 M NaCl. Protein impurities were further removed by gel filtration (HiLoad 26/60 Superdex 200 prep grade, GE Healthcare) equilibrated with 50 mM Tris-HCl pH 8 and 150 mM NaCl. The protein fractions were pooled, concentrated and stored at -80°C for crystallization assays. For RPE, DCS and ITC experiments, which are highly sensitive to metal trace, above purified RgFtrA and RgFtrB were treated with 50 mM ethylenediaminetetraacetic acid (EDTA) for 30 min. A desalting column allowed EDTA removing using 50 mM Tris-HCl pH 8 or MES pH 6.5 and 150 mM NaCl. The RgFtrA after EDTA treatment was loaded with equimolar $CuCl_2$ for DCS, ITC, RPE and crystallization assays.

**Cloning, expression and purification of 'as isolated' mature Strep-tag RgFtrA.** The synthetic gene (Genscript) coding for the mature RgFtrA protein fused to a C-terminal Strep-tag with its own promoter sequence was inserted in the puc57 plasmid at KpnI-XbaI sites. From this plasmid called puc57-*ftrAstreptag*, the tagged gene was subcloned into the replicative plasmid pBBR1MCS-2 at KpnI-XbaI sites. pBBR2-*ftrAstreptag* plasmid thus obtained was introduced by electroporation in the *ΔftrATp* mutant. Strep-tag RgFtrA protein was purified from *R. gelatinous ΔftrATp* mutant cells grown photosynthetically (2 L) for 48 h at 30°C in iron depleted medium. Cells were pelleted by centrifugation at 3,000 *g* for 15 min at 4°C. The bacterial pellet was washed with 0.1 M Tris-HCl pH 8 and 150 mM NaCl buffer and centrifuged. The bacterial pellet was fast frozen in liquid nitrogen before storage at -20°C. For cell lysis by sonication, the bacterial pellet was resuspended in 0.1 M Tris-HCl pH 8 and 150 mM NaCl, supplemented with 0.1 M of PMSF (phenylmethylsulfonyl fluoride) and DNAse 50 µg/mL. Lysed cells were centrifuged at 208,000 *g* for 90 min at 4°C. The soluble fraction was filtered before loaded onto a StrepTrapHP column (5ml, Merck). The proteins were eluted with 5 ml of 2.5 mM desthiobiotin. Protein fractions were loaded onto a gel filtration (HiLoad 26/60 Superdex 200 prep grade,

GE Healthcare) equilibrated with 50 mM Tris-HCl pH 8 and 150 mM NaCl. The protein fractions were concentrated on Amicon YM-10 (Millipore) concentrator pooled, and stored at -80°C.

**Crystallization and structure determination.** Crystallization conditions for His-tag RgFtrA, RgFtrA and Strep-tag RgFtrA were screened using QIAGEN kits (Valencia, CA) with a Mosquito nanodrop robot (SPT Labtech). His-tag RgFtrA and RgFtrA crystals were manually optimized in the same crystallization condition (Tables 1 and 2). Strep-tag RgFtrA crystals were obtained in three different conditions of polyethylene glycol with one condition containing 0.2 M $MgCl_2$ and were manually optimized. Few crystals of Strep-tag RgFtrA were soaked with 0.1 M $FeCl_3$ and turned orange. Co-crystallization of His-tag RgFtrA with 20 mM $NiSO_4$ was manually realized (Table S1). RgFtrA treated with EDTA and loaded with equimolar $CuCl_2$ and 1 mM $FeSO_4$ crystallized in the same condition containing $MgCl_2$ than the Strep-tag RgFtrA co-crystallized with 4 mM $FeSO_4$. Unfortunately, no iron was present in these co-crystal structures, instead magnesium ions were observed. Crystals were transferred to a cryo-protectant solution (mother liquor supplemented with 20% PEG 400 or 30% glycerol) and flash-frozen in liquid nitrogen. Diffraction data were collected at 100 K on PROXIMA 1 and 2 beamlines at SOLEIL synchrotron (Saint-Aubin, France). Data processing was performed using the XDS package [37] (Table 1 and 2). We determined first the structure of His-tag RgFtrA at 1.4 Å resolution by molecular replacement using the structure of *Campylobacter jejuni* P19 (CjP19 PDB 3LZL) as a search model. Because, the crystals of RgFtrA were isomorphous to those of His-tag RgFtrA, phases determination at 1.23 Å resolution was straightforward. Both His-tag and RgFtrA structures were empty. The presence of nickel in co-crystals of His-tag RgFtrA with 20 mM $NiSO_4$ was confirmed by an X-ray fluorescence emission scan on the beamline and a nickel anomalous data set at 1.379288 Å wavelength was collected at 1.8 Å resolution. A nickel ion is 50% present in only one subunit of the dimer. The three structures of the endogenous Strep-tag RgFtrA were determined by molecular replacement with PHASER [38] using the high resolution refined structure of RgFtrA as a search model. They contain a fully occupied endogenous copper ion in each subunit of the asymmetric unit. No iron was detected using X-ray fluorescence emission scan in the Strep-tag RgFtrA-iron co-crystals. The structure composed of three dimers in the asymmetric unit revealed the presence of a magnesium ion

originated from the crystallization conditions bound to the second metal site. Removing $MgCl_2$ prevented crystals growth. Two crystals of RgFtrA treated with EDTA and loaded with equimolar CuCl2 and 1 mM FeSO4 denoted X1 and X2 grown with 100 and 50 mM $MgCl_2$, respectively, were collected. Because of the anisotropy of the diffraction of X1 and X2 crystals as well as the Strep-tag RgFtrA crystal grown in $MgCl_2$, the DEBYE and STARANISO programs developed by Global phasing Ltd were applied to the data scaled with AIMLESS using the STARANISO server (http://staraniso.globalphasing.or/). These programs perform an anisotropic cut-off of merge intensity data on the basis of an analysis of local $I/\sigma(I)$, compute Bayesian estimates of structures amplitudes, taking into account their anisotropic fall-off, and apply an anisotropic correction to the data. The corrected anisotropic amplitudes were used for further refinement.

The presence of iron in soaked crystals of Strep-tag RgFtrA with 0.1 M $FeCl_3$ was confirmed by an X-ray fluorescence emission scan on the beamline and an iron anomalous data set at 1.73925 Å wavelength was collected at 2.75 Å resolution. An iron ion is present in each subunit of the dimer of the asymmetric unit.

Refinement of each structure was performed with BUSTER-2.10 [39], employing TLS groups and NCS restraints when more than one molecule was present in the asymmetric unit. Inspection of the density maps and manual rebuilding were performed using COOT [40]. Refinement details of each structure are shown in Tables 1 and 2. Molecular graphics images were generated using PyMOL (http://www.pymol.org).

**Electron paramagnetic resonance (EPR) measurement.** X-band cw-EPR spectra were recorded with a Bruker Elexsys 500 X-band spectrometer equipped with a standard ER 4102 (Bruker) X-band resonator, a Bruker teslameter, an Oxford Instruments cryostat (ESR 900) and an Oxford ITC504 temperature controller.

**Differential scanning calorimetry (DSC).** Thermal stability of the His-tag RgFtrA, the RgFtrA, the RgFtrA treated with EDTA and loaded with equimolar $CuCl_2$, the Strep-tag RgFtrA expressed in *R. gelatinosus* periplasm, and the RgFtrB treated with EDTA was performed by DSC on a MicroCal model

VP-DSC in a standard buffer with 30 µM and 300 µM for protein and metal, respectively. Divalent metals were used such as $MgSO_4$, $MnCl_2$, $NiSO_4$, CuCl, $CuCl_2$, $CoCl_2$, $CdCl_2$, $ZnSO_4$, $FeSO_4$, and $FeCl_3$. Each measurement was preceded by a baseline scan with the standard buffer. All solutions were degassed just before loading into the calorimeter. Scans were performed at 1 K.min$^{-1}$ between 20 and 90°C. The heat capacity of the buffer was subtracted from that of the protein sample before analysis. Thermodynamic parameters were determined by fitting the data to the following equation:

$$\Delta C_p(T) = \frac{K_d(T)\,\Delta H_{cal}\,\Delta H_{vH}}{[1+K_d(T)]^2\,RT^2}$$

where *K*d is the equilibrium constant for a two-state process, Δ*H*vh is the enthalpy calculated on the basis of a two-state process and Δ*H*cal is the measured enthalpy.

**Tycho NT.6 Nanotemper Differential Scanning Fluorimeter**. This equipment measures the change in intrinsic fluorescence of tryptophan residues in protein samples. Protein unfolding was followed by tryptophan fluorescence intensity at 330 and 350 nm in the presence of different metals (same as for DSC). The inflection temperature ($T_i$) was determined by detecting the maximum of the first derivative of the fluorescence ratios ($F_{350}/F_{330}$) after fitting experimental data with a polynomial function. Data were measured in triplicate. Tycho NT.6 was used with a heating rate of 30°C min$^{-1}$.

**Isothermal titration microcalorimetry measurements (ITC).** Isothermal titration microcalorimetry experiments were performed with an ITC200 isothermal titration calorimeter from MicroCal (Malvern). The experiments were carried out at 25°C. Protein concentration in the microcalorimeter cell (0.2 ml) was 50 µM. Nineteen injections of 2 µl metal at concentrations ranging from 700 to 800 µM were performed at intervals of 180 s while stirring at 500 rpm. The experimental data were fitted to theoretical titration curves with software supplied by MicroCal (ORIGIN®). This software uses the relationship between the heat generated by each injection and ΔH (enthalpy change in Kcal/Mol), $K_a$ (the association binding constant in M$^{-1}$), n (the number of binding sites), total protein concentration and free and total ligand concentrations [41].

**Accession numbers.** The atomic coordinates and structure factors have been deposited at the Protein Data Bank under PDB ID 7R3P and 7R4U for His-tag RgFtrA and RgFtrA respectively, PDB ID 7R3S for His-tag RgFtrA-$Ni^{2+}$, PDB ID 7R4V for Strep-tag RgFtrA-$Cu^{+}$, PDB ID 7R5P for Step-tag RgFtrA-$Cu^{+}Mg^{2+}$ , PDB ID 7R4Z for Step-tag RgFtrA-$Cu^{+}Fe^{3+}$ and PDB ID 7R5E and 7R5G for RgFtrA-$Cu^{2+}Mg^{2+}$ denoted X1 and X2 in Table 1, respectively

**Acknowledgements.** This work benefited from the I2BC crystallization and microcalorimetry platforms supported by FRISBI ANR-10-INSB-05-01. We acknowledge SOLEIL for provision of synchrotron radiation facilities (proposals ID 20170872 and 20191181) in using PROXIMA 1 and 2 beamlines and we thank all the staff for assistance in using the beamlines. The LABGeM (CEA/Genoscope & CNRS UMR8030), the France Génomique and French Bioinformatics Institute national infrastructures (funded as part of Investissement d'Avenir program managed by Agence Nationale pour la Recherche, contracts ANR-10-INBS-09 and ANR-11-INBS-0013) are acknowledged for support within the MicroScope annotation platform. We thank I2BC for its financial support from the inter-department call and Andrew Saurin for a critical reading.

**Author contributions.** ASS and SO performed the experiments on *R. gelatinosus*. SP and AV performed the crystallization assays. AV and SM performed the crystallography work. MAN and AB performed the DSC/microcalorimetry and EPR experiments, respectively. ASS and SM wrote the manuscript. All the authors discussed the results and contributed to the writing of the manuscript.

**Conflict of interest.** The authors declare no conflict of interest.

**References**


1 Grass G (2006) Iron Transport in Escherichia Coli: All has not been said and Done. *BioMetals* **19**, 159–172.

2 Krewulak KD & Vogel HJ (2008) Structural biology of bacterial iron uptake. *Biochim Biophys Acta BBA - Biomembr* **1778**, 1781–1804.

3 Schalk IJ, Mislin GLA & Brillet K (2012) Structure, Function and Binding Selectivity and Stereoselectivity of Siderophore–Iron Outer Membrane Transporters. In *Current Topics in Membranes* pp. 37–66. Elsevier.

4 Mietzner TA, Tencza SB, Adhikari P, Vaughan KG & Nowalk AJ (1998) Fe(III) Periplasm-to-Cytosol Transporters of Gram-Negative Pathogens. In *Bacterial Infection: Close Encounters at the Host Pathogen Interface* (Vogt PK & Mahan MJ, eds), pp. 113–135. Springer, Berlin, Heidelberg.

5 Parker Siburt CJ, Mietzner TA & Crumbliss AL (2012) FbpA — A bacterial transferrin with more to offer. *Biochim Biophys Acta BBA - Gen Subj* **1820**, 379–392.

6 Lau CKY, Krewulak KD & Vogel HJ (2016) Bacterial ferrous iron transport: the Feo system. *FEMS Microbiol Rev* **40**, 273–298.

7 Große C, Scherer J, Koch D, Otto M, Taudte N & Grass G (2006) A new ferrous iron-uptake transporter, EfeU (YcdN), from Escherichia coli. *Mol Microbiol* **62**, 120–131.

8 Rajasekaran MB, Nilapwar S, Andrews SC & Watson KA (2009) EfeO-cupredoxins: major new members of the cupredoxin superfamily with roles in bacterial iron transport. *BioMetals* **23**, 1–17.

9 Chan ACK, Doukov TI, Scofield M, Tom-Yew SAL, Ramin AB, MacKichan JK, Gaynor EC & Murphy MEP (2010) Structure and Function of P19, a High-Affinity Iron Transporter of the Human Pathogen Campylobacter jejuni. *J Mol Biol* **401**, 590–604.

10 Brickman TJ & Armstrong SK (2012) Iron and pH-responsive FtrABCD ferrous iron utilization system of *Bordetella* species: *Bordetella* ferrous iron transport system. *Mol Microbiol* **86**, 580–593.

11 Elhassanny AEM, Anderson ES, Menscher EA & Roop RM (2013) The ferrous iron transporter FtrABCD is required for the virulence of *Brucella abortus* 2308 in mice: Ferrous iron transport and virulence in *Brucella*. *Mol Microbiol* **88**, 1070–1082.

12 Miethke M, Monteferrante CG, Marahiel MA & van Dijl JM (2013) The Bacillus subtilis EfeUOB transporter is essential for high-affinity acquisition of ferrous and ferric iron. *Biochim Biophys Acta BBA - Mol Cell Res* **1833**, 2267–2278.

13 Mathew A, Eberl L & Carlier AL (2014) A novel siderophore-independent strategy of iron uptake in the genus *B urkholderia*: Siderophore-independent iron uptake in *Burkholderia*. *Mol Microbiol* **91**, 805–820.

14 Butt AT & Thomas MS (2017) Iron Acquisition Mechanisms and Their Role in the Virulence of Burkholderia Species. *Front Cell Infect Microbiol* **7**.

15 Banerjee S, Chanakira MN, Hall J, Kerkan A, Dasgupta S & Martin DW (2022) A review on bacterial redox dependent iron transporters and their evolutionary relationship. *J Inorg Biochem* **229**, 111721.

16 Stearman R, Yuan DS, Yamaguchi-Iwai Y, Klausner RD & Dancis A (1996) A permease-oxidase complex involved in high-affinity iron uptake in yeast. *Science* **271**, 1552–1557.

17 Severance S, Chakraborty S & Kosman DJ (2004) The Ftr1p iron permease in the yeast plasma membrane: orientation, topology and structure-function relationships. *Biochem J* **380**, 487–496.

18 Singh A, Severance S, Kaur N, Wiltsie W & Kosman DJ (2006) Assembly, Activation, and Trafficking of the Fet3p·Ftr1p High Affinity Iron Permease Complex in Saccharomyces cerevisiae. *J Biol Chem* **281**, 13355–13364.

19 Cao J, Woodhall MR, Alvarez J, Cartron ML & Andrews SC (2007) EfeUOB (YcdNOB) is a tripartite, acid-induced and CpxAR-regulated, low-pH Fe2+ transporter that is cryptic in Escherichia coli K-12 but functional in E. coli O157:H7. *Mol Microbiol* **65**, 857–875.
20 Rajasekaran MB, Nilapwar S, Andrews SC & Watson KA (2010) EfeO-cupredoxins: major new members of the cupredoxin superfamily with roles in bacterial iron transport. *BioMetals* **23**, 1–17.
21 Liu MM, Boinett CJ, Chan ACK, Parkhill J, Murphy MEP & Gaynor EC (2018) Investigating the *Campylobacter jejuni* Transcriptional Response to Host Intestinal Extracts Reveals the Involvement of a Widely Conserved Iron Uptake System. *mBio* **9**.
22 De Silva DM, Askwith CC, Eide D & Kaplan J (1995) The FET3 Gene Product Required for High Affinity Iron Transport in Yeast Is a Cell Surface Ferroxidase. *J Biol Chem* **270**, 1098–1101.
23 Steunou AS, Bourbon M-L, Babot M, Durand A, Liotenberg S, Yamaichi Y & Ouchane S (2020) Increasing the copper sensitivity of microorganisms by restricting iron supply, a strategy for bio-management practices. *Microb Biotechnol* **13**, 1530–1545.
24 Hassani BK, Steunou A-S, Liotenberg S, Reiss-Husson F, Astier C & Ouchane S (2010) Adaptation to oxygen: role of terminal oxidases in photosynthesis initiation in the purple photosynthetic bacterium, Rubrivivax gelatinosus. *J Biol Chem* **285**, 19891–19899.
25 Steunou AS, Bourbon M-L, Babot M, Durand A, Liotenberg S, Yamaichi Y & Ouchane S (2020) Increasing the copper sensitivity of microorganisms by restricting iron supply, a strategy for bio-management practices. *Microb Biotechnol*, 1530–1545.
26 Holmes K, Mulholland F, Pearson BM, Pin C, McNicholl-Kennedy J, Ketley JM & Wells JM (2005) Campylobacter jejuni gene expression in response to iron limitation and the role of Fur. *Microbiology* **151**, 243–257.
27 Kammler M, Schön C & Hantke K (1993) Characterization of the ferrous iron uptake system of Escherichia coli. *J Bacteriol* **175**, 6212–6219.
28 Carpenter C & Payne SM (2014) Regulation of iron transport systems in Enterobacteriaceae in response to oxygen and iron availability. *J Inorg Biochem* **133**, 110–117.
29 Chan ACK, Lin H, Koch D, Grass G, Nies DH & Murphy MEP (2020) A copper site is required for iron transport by the periplasmic proteins P19 and FetP. *Met Integr Biometal Sci* **12**, 1530–1541.
30 Dudek C-A & Jahn D (2022) PRODORIC: state-of-the-art database of prokaryotic gene regulation. *Nucleic Acids Res* **50**, D295–D302.
31 Janin J, Rodier F, Chakrabarti P & Bahadur RP (2007) Macromolecular recognition in the Protein Data Bank. *Acta Crystallogr D Biol Crystallogr* **63**, 1–8.
32 Koch D, Chan ACK, Murphy MEP, Lilie H, Grass G & Nies DH (2011) Characterization of a dipartite iron uptake system from uropathogenic Escherichia coli strain F11. *J Biol Chem* **286**, 25317–25330.
33 Page C (2003) Mechanism for electron transfer within and between proteins. *Curr Opin Chem Biol* **7**, 551–556.
34 Sambrook J, Fritsch ER & Maniatis T (1989) *Molecular Cloning: A Laboratory Manual (2nd ed.)*, Cold Spring Harbor Laboratory Press.
35 Azzouzi A, Steunou A-S, Durand A, Khalfaoui-Hassani B, Bourbon M, Astier C, Bollivar DW & Ouchane S (2013) Coproporphyrin III excretion identifies the anaerobic coproporphyrinogen III oxidase HemN as a copper target in the Cu+-ATPase mutant copA− of Rubrivivax gelatinosus. *Mol Microbiol*. **88**, 339-351.

36 Liotenberg S, Steunou A-S, Picaud M, Reiss-Husson F, Astier C & Ouchane S (2008) Organization and expression of photosynthesis genes and operons in anoxygenic photosynthetic proteobacteria. *Environ Microbiol* **10**, 2267–2276.
37 Kabsch W (2010) *XDS*. *Acta Crystallogr D Biol Crystallogr* **66**, 125–132.
38 McCoy AJ, Grosse-Kunstleve RW, Adams PD, Winn MD, Storoni LC & Read RJ (2007) Phaser crystallographic software. *J Appl Crystallogr* **40**, 658–674.
39 Blanc E, Roversi P, Vonrhein C, Flensburg C, Lea SM & Bricogne G (2004) Refinement of severely incomplete structures with maximum likelihood in BUSTER–TNT. *Acta Crystallogr D Biol Crystallogr* **60**, 2210–2221.
40 Emsley P & Cowtan K (2004) Coot: model-building tools for molecular graphics. *Acta Crystallogr D Biol Crystallogr* **60**, 2126–2132.
41 Wiseman T, Williston S, Brandts JF & Lin L-N (1989) Rapid measurement of binding constants and heats of binding using a new titration calorimeter. *Anal Biochem* **179**, 131–137.

**Table 1**. Crystallographic data and refinement parameters.

| | apo RgFtrA | Strep-tag RgFtrA-$Cu^{+}$ | Strep-tag RgFtrA-$Cu^{+}Fe^{3+}$ |
|---|---|---|---|
| PDB code | **7R4U** | **7R4V** | **7R4Z** |
| Wavelength (Å) | 0.979336 | 1.379288 | 1.73925 |
| Crystallization conditions | 2 M AS, 0.1 M NaCitrate pH 5.6 | 20% PEG 1500 0.1 M HEPES pH 7.5 | 20% PEG 2K MME 0.1 M tris-HCl pH 8.5 0.2 soaked with 0.1 M $FeCl_3$. |
| *Za* | 2 | 2 | 2 |
| Number of amino-acids Chains A/B | 156/163 | 154/156 | 156/156 |
| Space group Cell parameters (Å,°) | $P2_12_12_1$ a= 59.3 b= 79.9 c= 82.8 | $P2_12_12_1$ *a*= 61.4 *b*= 65.9 *c*= 70.1 | $P2_12_12_1$ *a*= 60.8 *b*= 71.2 *c*= 79.6 |
| Resolution (Å) | 48.25-1.23 (1.3-1.23) | 49-1.3 (1.38-1.3) | 2.75 (2.92-2.75) |
| No. of observed reflections | 1460931 (179016) | 676517 (14178) | 52608 (3155) |
| No. of unique reflections | 114401 (17537) | 114500 (6218) | 8992 (1137) |
| Completeness (%) | 98.9 (94.9) | 84.6 (28.5) | 95.3 (76.7) |
| $R_{sym}$ (%) | 6.7 (200.9) | 7.7 (54.9) | 18.3 (93) |
| $R_{pim}$ (%) | 2.7 (112.4) | 3.3 (51.8) | 10.2 (87.8) |
| $I/\sigma(I)$ | 18.9 (1.05) | 15.1 (1.15) | 9.6 (1.21) |
| $CC_{1/2}$ | 1 (0.424) | 0.998 (0.633) | 0.993 (0.515) |
| $R_{cryst}$ (%) | 17 | 17.2 | 17.1 |
| $R_{free}$ (%) | 18.6 | 19.2 | 22.8 |
| rms bond deviation (Å) | 0.01 | 0.009 | 0.01 |
| rms angle deviation (°) | 1.07 | 1.13 | 1.11 |
| Average B (Å$^2$) Protein A/B $Cu^{+}$ A/B $Fe^{3+}$ A/B solvent | 19.3/21.8 36.7 | 15.7/16.6 11.1/11.8 27.3 | 56/59 72.4/60.7 60/58.8 47.5 |
| [a]Clashscore MolProbity score | 1.14 0.82 | 2 0.97 | 0.83 1.17 |
| [a]Ramachandran plot (%) Favoured Outliers | 99.68 0 | 99.02 0 | 98.38 0 |

Values for the highest resolution shell are in parentheses
$CC_{1/2}$ = percentage of correlation between intensities from random hall-dataset
[a]Calculated with MolProbity

**Table 2**. Crystallographic data and refinement parameters.

| | His-tag apo RgFtrA | His-tag RgFtrA-$Ni^{2+}$ | RgFtrA-$Cu^{2+}Mg^{2+}$ (X1) | RgFtrA-$Cu^{2+}Mg^{2+}$ (X2) | Strep-tag RgFtrA-$Cu^{+}Mg^{2+}$ |
|---|---|---|---|---|---|
| PDB code | **7R3P** | **7R3S** | **7R5E** | **7R5G** | **7R5P** |
| Wavelength (Å) | 0.978566 | 1.48484 | 1.73114 | 1.73114 | 0.980115 |
| Crystallization conditions | 2 M AS, 0.1 M Citrate Sodium pH5.6 | 2 M AS, 0.1 M Citrate Sodium pH5.6 0.02 M $NiSO_4$ | 25% PEG 4K, 0.1 M Tris-HCl pH 8.5 0.1 M $MgCl_2$ | 25% PEG 4K, 0.1 M Tris-HCl pH 8.5 0.05 M $MgCl_2$ | 25% PEG 4K, 0.1 M Tris-HCl pH 8.5 0.2 M $MgCl_2$ |
| *Za* | 2 | 2 | 2 | 2 | 6 |
| Number of aminoacids Chains A/B/C/D/E/F | 157/157 | 157/157 | 156/156 | 156/155 | 156/156/154/156/156/155 |
| Space group Cell parameters (Å,°) | $P2_12_12_1$ *a*= 59.2 *b*= 80.3 *c*= 82.9 | $P2_12_12$ *a*= 59.3 *b*= 79.8 *c*= 82.4 | *C2* *a*= 92.6 *b*= 48.9 *c*= 78.2 β= 123.1 | *C2* *a*= 92.6 *b*= 48.4 *c*= 78.6 β= 123.8 | $P2_1$ *a*= 47.5 *b*= 77.9 *c*= 115.2 β= 95.8 |
| Resolution (Å) | 48.1-1.4 (1.48-1.4) | 49.13-1.8 (1.9-1.8) | 27.4-2.2 (2.27-2.2) | 41.08-2.2 (2.23-2.2) | 49-1.68 (1.86-1.68) |
| No. of observed reflections | 1049112 (160830) | 426698 (31633) | 59199 (1111) | 71689 (2428) | 598262 (18238) |
| No. of unique reflections | 78363 (12299) | 68702 (10524) | 14345 (523) | 15041 (711) | 92927 (4342) |
| Completeness (%) | 99.7(97.9) | 99.8 (56.1) | 98.5 (69.4) | 99.7 (75.3) | 99.5 (94) |
| Completeness Staraniso (%) | | | *98.5 (64.9)* | *99.7 (50.4)* | *94 (63.1)* |
| $R_{sym}$ (%) | 8.6 (126.2) | 7.8 (70.7) | *12.8 (55.4)* | *6.7 (50.6)* | *7.7 (73.8)* |
| $R_{pim}$ (%) | 2.4 (36.9) | 7.5 (37.3) | *6.7 (37.6)* | *3.3 (27.3°* | *3.2 (36.9)* |
| $I/\sigma(I)$ | 15.9 (1.58) | 12.2 (1.17) | *8.9 (2.5)* | *11 (2.8)* | *11.4 (1.7)* |
| $CC_{1/2}$ | 0.999(0.718) | 0.998 (0.561) | *0.985(0.649)* | *0.997(0.873)* | *0.998 (0.725)* |
| $R_{cryst}$ (%) | 17.8 | 17.6 | 17.6 | 17.2 | 17.9 |
| $R_{free}$ (%) | 19.1 | 20.1 | 21.7 | 19.6 | 21.1 |
| rms bond deviation (Å) | 0.01 | 0.01 | 0.01 | 0.01 | 0.01 |
| rms angle deviation (°) | 1.1 | 1.07 | 1.11 | 1.08 | 1.04 |
| Average B ($Å^2$) | | | | | |
| Protein A/B/C/D/EF | 22.4/26 | 36/40.7 | 23.9/22.2 | 31.4/40.4 | 29/29/38.7/34/30.7/36 |
| Cu A/B/C/D/E/F | | | 14.4/15.3 | 23.3/23.9 | 18.5/18.6/25.8/23.6/20.3/23.7 |
| $Ni^{2+}$ A | | 33.8 | | | |
| $Mg^{2+}$ A/B/C/D/E/F | | | 34/40.1 | 61/65.9 | 27.4/47.5/55.6/55.6/37.5/25.3/46.9 |
| $Mg^{2+}$ in solvent | | | 25.4 | | |
| solvent | 39 | 48.4 | 24.3 | 35 | 33.7 |
| [a]Clashscore | 0.98 | 1.57 | 1.44 | 1.04 | 1.38 |
| MolProbity score | 0.79 | 0.93 | 1.16 | 0.8 | 0.98 |
| [a]Ramachandran plot (%) | | | | | |
| Favoured | 99.03 | 98.4 | 99.35 | 99.35 | 98.69 |
| Outliers | 0 | 0 | 0 | 0 | 0 |

Values for the highest resolution shell are in parentheses

$CC_{1/2}$ = percentage of correlation between intensities from random hall-dataset

[a]Calculated with MolProbity

**Table 3.** *Tm* of RgFtrA devoid of any metal without and with different cations in the primary metal binding site using DSC (see supplementary Figure S3). *Tm* of RgFtrA devoid of any metal and loaded with equimolar $CuCl_2$ with different cations in the secondary metal binding site using DSC at pH 6.5 (see supplementary Figure S6).

| | ***Tm* (°C)** | **Δ*Tm* (°C)** | **$\Delta H_1$ (kcal/mol)** | **$\Delta HVH_1$ (kcal/mol)** |
|---|---|---|---|---|
| **RgFtrA** | 52.06 | | 167 | 199 |
| + $MnCl_2$ | 55.20 | 3.14 | 190 | 214 |
| + $MgCl_2$ | 52.45 | 0.39 | 175 | 204 |
| + $FeSO_4$ | 53.53 | 1.47 | 155 | 134 |
| + $FeCl_3$ | 53.37 | 1.31 | 152 | 166 |
| + CuCl | **76.78** | 24.72 | 155 | 137 |
| + $CuCl_2$ | **75.94** | 23.88 | 110 | 111 |
| + $NiSO_4$ | 72.34 | 20.28 | 85.4 | 139 |
| + $CdCl_2$ | 61.96 | 9.9 | 101 | 132 |
| + $ZnSO_4$ | 59.02 | 6.96 | 78.6 | 136 |
| + $CoCl_2$ | 58.59 | 6.53 | 81.2 | 120 |
| **RgFtrA-$CuCl_2$** | 72.98 | | 145 | 93.9 |
| + $MnCl_2$ | 75.44 | 2.46 | 152 | 109 |
| + $MgCl_2$ | 72.44 | -0.54 | 118 | 86.5 |
| + $CoCl_2$ | 74.21 | 1.23 | 137 | 111 |
| + $FeSO_4$ | **87.78** | 14.8 | 66 | 228 |
| + $FeCl_3$ | **87.38** | 14.4 | 66 | 207 |

**Table 4.** Distances in Å between copper (or nickel) ion and RgFtrA amino acids of the primary metal site. H131' belongs to the neighbouring subunit. Distances (below 3Å) between metal ion ($Fe^{3+}$ or $Mg^{2+}$) in the secondary metal site and RgFtrA amino acids or water molecules (W).

| | **His41** | **Met88** | **His95** | **His131'** | ***Glu43*** |
|---|---|---|---|---|---|
| **$Cu^{+}$ in strep-tag RgFtrA** | | | | | |
| (chain A) | 2.0 | 2.3 | 2.1 | 2.1 | *4* |
| (chain B) | 2.0 | 2.3 | 2.0 | 2.1 | *4* |
| **$Cu^{+}$ in strep-tag RgFtrA-CuFe** | | | | | |
| (chain A) | 2.4 | 2.3 | 2.2 | 2.2 | *4.3* |
| (chain B) | 2.3 | 2.3 | 2.0 | 2.2 | *4.4* |
| **$Cu^{+}$ in strep-tag RgFtrA-CuMg** | | | | | |
| (chain A) | 2.1 | 2.4 | 2.0 | 2.1 | *3.8* |
| (chain B) | 2.1 | 2.3 | 2.1 | 2.1 | *4.0* |
| (chain C) | 2.2 | 2.3 | 2.2 | 2.1 | *4.0* |
| (chain D) | 2.2 | 2.3 | 2.1 | 2.1 | *3.8* |
| (chain E) | 2.1 | 2.3 | 2.0 | 2.2 | *3.8* |
| (chain F) | 2.1 | 2.3 | 2.1 | 2.1 | *3.8* |
| **$Cu^{2+}$ in RgFtrA-CuMg (X1)** | | | | | |
| (chain A) | 2.1 | 2.4 | 2.2 | 2.2 | *3.9* |
| (chain B) | 2.2 | 2.2 | 2.2 | 2.2 | *4.8* |
| **$Cu^{2+}$ in RgFtrA-CuMg (X2)** | | | | | |
| (chain A) | 2.1 | 2.3 | 2.1 | 2.2 | *3.7* |
| (chain B) | 2.1 | 2.3 | 2.1 | 2.2 | *5.4* |
| **$Ni^{2+}$ in his-tag RgFtrA** | 2.4 | 3.2 | 1.7 | 2.4 | *2.7* |

**Table 5.** Distances (below 2.5 Å) between metal ion ($Fe^{3+}$ or $Mg^{2+}$) in the secondary metal site and RgFtrA amino acids or water molecules (W).

| | **Glu2** | **Glu43** | **Asp92** | W | W | W | W |
|---|---|---|---|---|---|---|---|
| **$Fe^{3+}$** | | | | | | | |
| (chain A) | 2.3 | 2.2 | 1.7 | 2.6 | 3 | | |
| (chain B) | 2.3 | 2.2 | 1.9 | | | | |
| **$Mg^{2+}$ (PDB 7R5E)** | | | | | | | |
| (chain A) | 3 | 2.7 | 2.0 | 2.7 | | | |
| (chain B) | 2.5 | 2.2 | 2.3 | | | | |
| **$Mg^{2+}$(PDB 7R5G)** | | | | | | | |
| (chain A) | 3 | 2.6 | 2.2 | 2.6 | | | |
| (chain B) | | 2.8 | 2.1 | 2.7 | | | |
| **$Mg^{2+}$ (PDB 7R5P)** | | | | | | | |
| (chain A) | | 2.3 | 2.1 | 2.2 | 2.0 | 2.0 | 2.2 |
| (chain B) | | 2.4 | 2.2 | 2.2 | 1.9 | 1.9 | 2.3 |
| (chain E) | | 2.2 | 2.2 | 2.1 | 2.1 | 1.9 | 2.3 |
| (chain D) | | 2.3 | 2.3 | 2.2 | 2.2 | | 2.4 |
| (chain C) | | 2.2 | 2.1 | | | | |
| (chain F) | | 2.3 | 2.2 | 2.3 | | 2.0 | 2.3 |

**Figure legends**

**Figure 1. (A)** A schematic representation of the ferrous iron uptake Ftr1-like system from *Rubrivivax gelatinosus*. **(B)** Organization of the *ftrAPBCD* operon presented as orange arrows and position of Fur and FNR binding sites in the promoter region. The operon is composed of 5 genes coding for the periplasmic FtrA, the porine FrtP, the CupII-type ferroxidase FtrB, the transporter FtrC (Ftr1p homolog) and the putative membrane polyferredoxin FtrD involved in the electron transfer. **(C)** Transcript level of *ftr* genes in the WT and *Δfnr* mutant of *R. gelatinosus* grown with (M) and without iron (–Fe) under aerobic (AE), microaerobic (MA) and photosynthesis anaerobic (PS) conditions. RT-PCR was performed to examine (i) the co-transcription of the *ftr* genes (ftrD reverse primer was used for the CDNA synthesis) (ii) genes regulation by oxygen concentration through FNR and (iii) by iron through Fur.

**Figure 2.** Growth comparison between the WT (red), *fbpAKm* (blue), Δ*ftrATp* (green), *ffA* (*fbpAKm-*Δ*ftrATp)* (purple) at pH 6 and pH 7 grown in iron-depleted malate medium microaerobic conditions. Results are the average of 3 independent experiments.

**Figure 3. (A)** Ribbon representation of the RgFtrA dimer and a close-up view of the water molecule (red sphere) bound to the primary metal site. Amino-acids are labelled and water-side chains interactions are shown as dashed red lines. **(B)** Superposition of the primary metal site of apo structures: RgFtrA (cyan), CjP19 (grey) with a 10% bound $Zn^{2+}$ (grey sphere) described as an apo form and apo EcFetP (yellow). The conserved amino acids forming the primary metal site are labelled and metal-CjP19 interactions are shown as plain grey lines. His95 in RgFtrA adopts a different position with the side chain out of the copper site. (**C**) Ribbon representation of the 'as isolated' Strep-tag RgFtrA dimer with an endogenous $Cu^{+}$ (purple sphere) bound the primary metal site and a close-up view of the RgFtrA-$Cu^{+}$ interactions. Amino-acids are labelled and metal-side chains interactions are shown as dashed lines. (**D**) Superposition of the copper binding site of 'as isolated' Strep-tag RgFtrA (purple) and RgFtrA (cyan). The conserved amino acids forming the primary metal site are labelled. The water molecule in

the RgFtrA is shown in red sphere and is at 1.8 Å of the $Cu^{+}$ ion. Molecular graphics were generated using PyMOL (http://www.pymol.org).

**Figure 4**. Isothermal titration microcalorimetry experiments for $K_D$ measurement of the RgFtrA-$Cu^{2+}$ complex towards $Fe^{2+}$ ions bound to the secondary metal site in MES at pH 6.5 (**A**) and in Tris-HCl at pH 8 (**B**). The top panel shows heat differences upon injection of metal ion and low panel shows integrated heats of injection with the best fit (solid line) to a single binding model using Microcal ORIGIN. ITC experiments were performed twice.

**Figure 5**. Isothermal titration microcalorimetry experiments for $K_D$ measurement of the RgFtrA-$Cu^{2+}$ complex towards $Fe^{2+}$ ions bound to the secondary metal site in MES at pH 6.5 (A) and in Tris-HCl at pH 8 (B). A control experiment of 1mM FeSO4 without protein was measured in MES at pH 6.5 (A). The top panel shows heat differences upon injection of metal ion and low panel shows integrated heats of injection with the best fit (solid line) to a single binding model using Microcal ORIGIN. ITC experiments were performed twice.

**Figure 6**. Differential scanning calorimetry thermograms of 'as isolated' Strep-tag RgFtrA expressed in *R. gelatinosus* with and without ethylenediaminetetraacetic acid (EDTA). The table below indicates the *Tm*. DSC experiments were performed twice. (**B**) Electron paramagnetic resonance spectrum recorded on 'as isolated' Strep-tag RgFtrA (80 µM) expressed in *R. gelatinosus* periplasm. The inset spectrum was recorded after the addition of a concentrated HCl (~ 18%) directly into the EPR tube. Temperature, 15 K; modulation amplitude, 25 G; microwave power, 20 mW; microwave frequency, 9.49 GHz; modulation frequency, 100 kHz. Inset: Temperature, 30 K; modulation amplitude, 25 G; microwave power, 5 mW; microwave frequency, 9.49 GHz; modulation frequency, 100 kHz.

**Figure 7. (A)** A close-up view of the His-tag RgFtrA-$Ni^{2+}$ interactions. Amino-acids are labelled and metal-side chains interactions are shown as plain green lines. $Ni^{2+}$ (green sphere) occupancy is 50% in line with the His95 side chain, observed in two positions as shown in the 2Fo-Fc electron density map contoured at 1σ: one allowing metal interaction and the other observed in apo RgFtrA. **(B)** Superposition of the copper binding site of 'as isolated' Strep-tag RgFtrA (purple) and His-tag RgFtrA-$Ni^{2+}$ (green).

The conserved amino acids forming the primary metal site are labelled. **(C)** Structural comparison of the two subunits of His-tag RgFtrA-Ni2+ dimer. A nickel ion (green sphere) occupies the primary metal site at 50% occupancy in subunit A (lime green) while a water molecule (red sphere) is present in subunit B (pink). Amino acids forming the primary metal site are labelled. Interactions between His-tag RgFtrA and nickel ion are shown as plain green lines whereas water-side chains interactions are shown as dashed red lines. Molecular graphics were generated using PyMOL (http://www.pymol.org).

**Figure 8. (A)** Ribbon representation of 'as-isolated' Strep-tag RgFtrA dimer in complex with ferric iron and a close-up view of the $Fe^{3+}$ (orange sphere) bound to the secondary metal site. Amino-acids are labelled and metal-side chains interactions are shown as plain orange lines **(B)** A different view of the same dimer as in **(A)** showing the $Fe^{3+}$ exposed at the protein surface. **(C)** Close up view of the two metal binding sites of the Strep-tag RgFtrA-$Cu^{+}Fe^{3+}$ complex (purple and orange spheres for Cu and Fe respectively). The two metal sites are separated by 7 Å. **(D)** Close up view of the two metal binding sites of the 'Strep-tag RgFtrA-$Cu^{+}Mg^{2+}$ complex. The two metal sites are separated by 6.7 Å. **(E)** Close-up view of the superimposed iron binding sites of the Strep-tag RgFtrA-$Cu^{+}Fe^{3+}$ and Strep-tag RgFtrA-$Cu^{+}Mg^{2+}$ complexes. Molecular graphics were generated using PyMOL (http://www.pymol.org).

**Figure 9.** EPR spectra recorded in the RgFtrA protein in a medium containing 50 mM MES and 150 mM NaCl at pH 6.5. In the four spectra, the RgFtrA concentration was 118 µM. The black spectrum corresponds to the "as purified" protein and was similar to that from the RgFtrA treated with EDTA. The red spectrum was recorded with the copper reconstituted protein. The blue spectrum was recorded with the copper reconstituted protein after the addition of 118 µM $FeSO_4$ directly in the EPR tube (from a stock at 1 mM $FeSO_4$ dissolved in water). The green spectrum was recorded with the copper reconstituted protein after the addition of 236 µM $FeSO_4$ directly in the EPR tube. The amplitude of the $Fe^{3+}$ EPR signal did not increase upon the addition of 236 µM FeSO4 when compared to the addition of 118 µM FeSO4 showing that there was no detectable auto oxidation of the $Fe^{2+}$ in these conditions. Instrument settings: Temperature, 15 K; modulation amplitude, 25 G; microwave power, 5 mW; microwave frequency, 9.49 GHz; modulation frequency, 100 kHz.

**Figure 10.** Differential scanning calorimetry thermograms of the RgFtrB with $CuCl_2$ and $FeSO_4$. The table below indicates the *Tm*. DSC experiments were performed twice.

**Figure 11.** Fnr (grey boxes) were found with PRODORIC database (https://www.prodoric.de/vfp/) in the promoter region of genes encoding the Ftr1P system from analyzed bacteria including *R. gelatinosus* (*R. gel*), *Magnetospirullum magneticum* (*M. mag*), *Escherichia coli* (*E. col*), *Campylobacter jejuni* (*C. jeu*), *Brucella abortus* (*B. abo*), *Bordetella pertussis* (*B. per*), *Pseudomonas syringae* (*P. syr*), *Rhodopseudomonas. palustris* (*R. pal*) or *Bacillus subtilis* (*B. sub*).

**Figure 12. (A)** Structure-based sequence alignment generated using Clustal Omega (https://www.ebi.ac.uk/Tools/msa/clustalo), manually corrected using COOT [40] and finalized using ESPript3 (https://espript.ibcp.fr/ESPript/ESPript) of RgFtrA (PDB 7R4Z) with CjP19 (PDB 3LZN) and EcFetP (PDB 3NRP). The secondary structure elements of RgFtrA (conserved in CjP19 and EcFetP) are labelled and indicated by coils for α-helices, arrow for β-strands and η for short $3_{10}$ helices. Identical residues are shown as white letters on a red background. The positions of the RgFtrA amino acids involved in copper (His41, Met88, His95 and His131) and in iron (Glu2, Glu43 and Asp92) binding are indicated by green and red triangles, respectively. These residues are all conserved. **(B)** Structural comparison between 'as isolated' Strep-tag RgFtrA and CjP19 (PDB 5I0V) in complex with copper and ferric iron. Copper and iron are represented by sphere and indicated. Molecular graphic was generated using PyMOL (http://www.pymol.org).

**Figure 13**. **(A)** Sequence alignment generated using Clustal Omega (https://www.ebi.ac.uk/Tools/msa/clustalo) and ESPript3 (https://espript.ibcp.fr/ESPript/ESPript) of RgFtrB with Bortedella and Brucella homologues shown with their accession number from Protein Blast-NCBI (https://blast.ncbi.nlm.nih.gov). Identical residues are shown as white letters on a red background. The conserved acidic residues at positions 42, 44, 51, 77 and 76 are indicated by red stars. (B) Ribbon representation of the predicted structure of RgFtrB from AlphaFold2 (ColaFold on google). The conserved acidic residues at positions 42, 44, 51, 77 and 76 are labelled and their side chains are shown in red. Molecular graphic was generated using PyMOL (http://www.pymol.org).

**Figure 14**. A proposed model for the ferrous iron transporter, FtrAPBCD from *R. gelatinosus*. Ferrous ion enters the periplasm through the porin FtrP localized in the outer membrane of the cells. It is sequestered by the periplasmic copper dependent ferrous iron oxydase FtrA. Then, the oxidized iron is taken in charge by the chaperon FtrB, which delivers the ferric iron to the permease FtrC for transport into the cytoplasm. The electrons from the iron oxidation by copper in FtrA are recycled by the polyferredoxin FtrD acting as the electron sink and resetting the ferrous uptake system.

**Supporting Information:**

Table S1. Bacterial strains and plasmids.

Table S2. Primers used in this work.

Figure S1. Growth of different single and double mutants.

Figure S2. Differential scanning calorimetry thermograms of RgFtrA and His-tag RgFtrA

Figure S3. Differential scanning calorimetry thermograms of RgFtrA devoid of any metal without and with different cations.

Figure S4. Effect of metal presence on the thermal unfolding of RgFtrA devoid of any metal without and with different cations.

Figure S5. Differential scanning calorimetry thermograms of the apo RgFtrA loaded with equimolar CuCl2 with different cations.

Figure S6. Effect of metal presence on the thermal unfolding RgFtrA-$Cu^{2+}$ with different cations measured by nanoDSF.

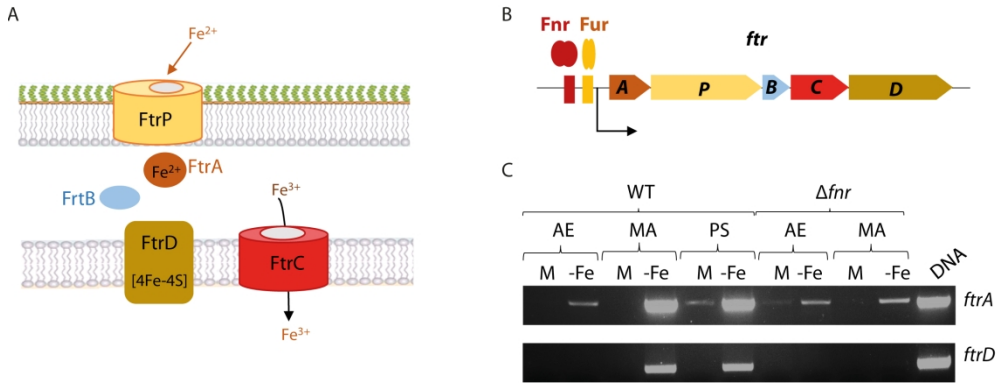



Figure 1

210x80mm (300 x 300 DPI)

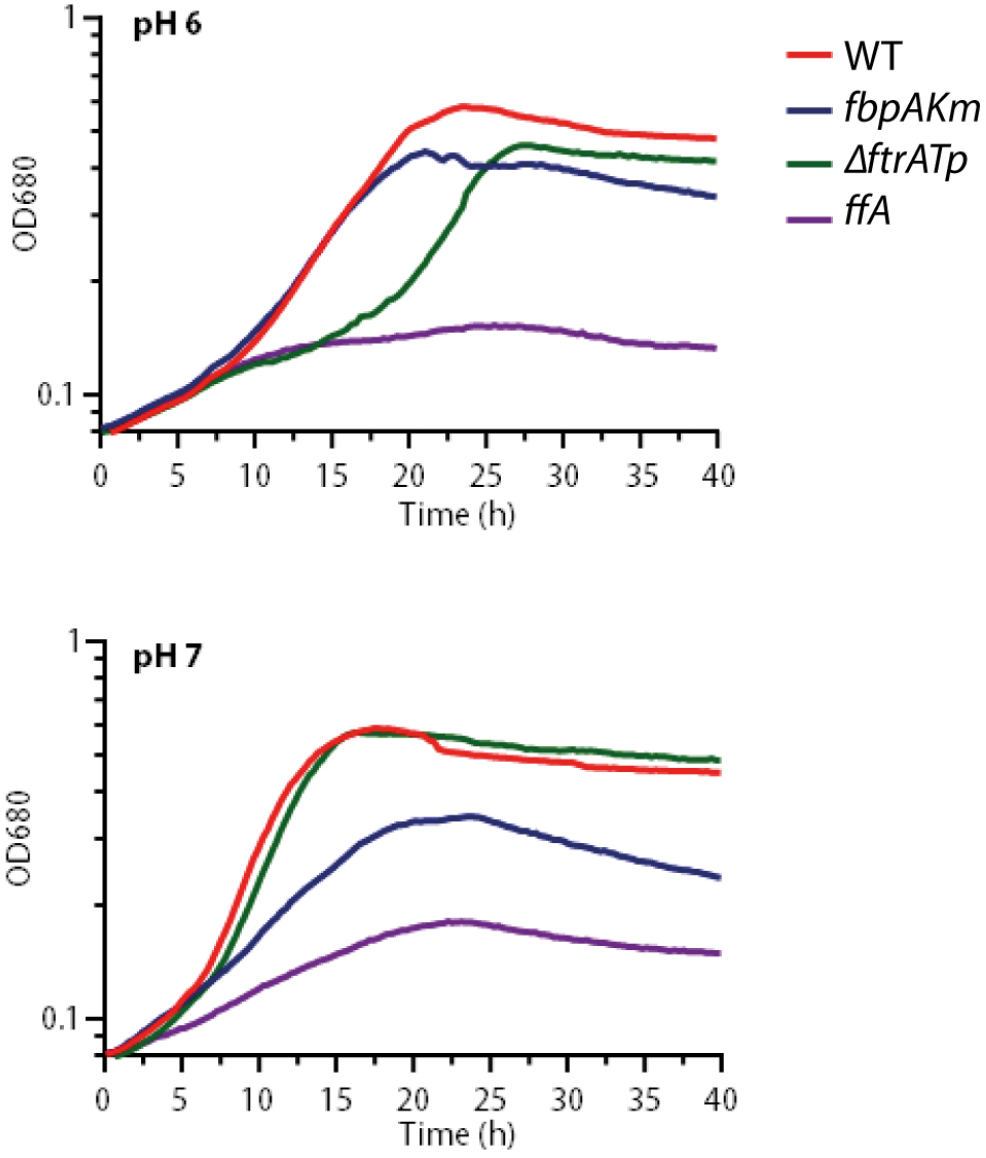



Figure 2

81x98mm (300 x 300 DPI)

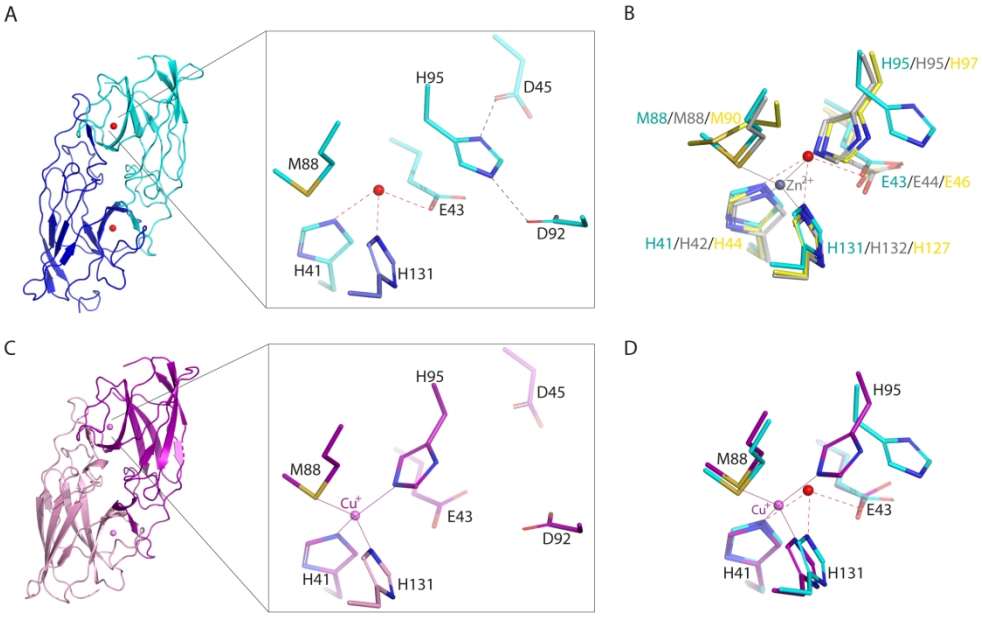
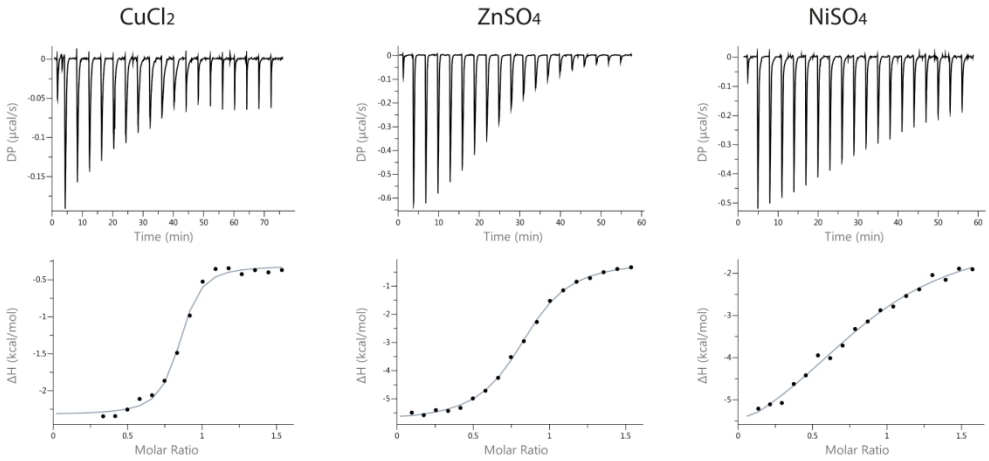



Figure 3

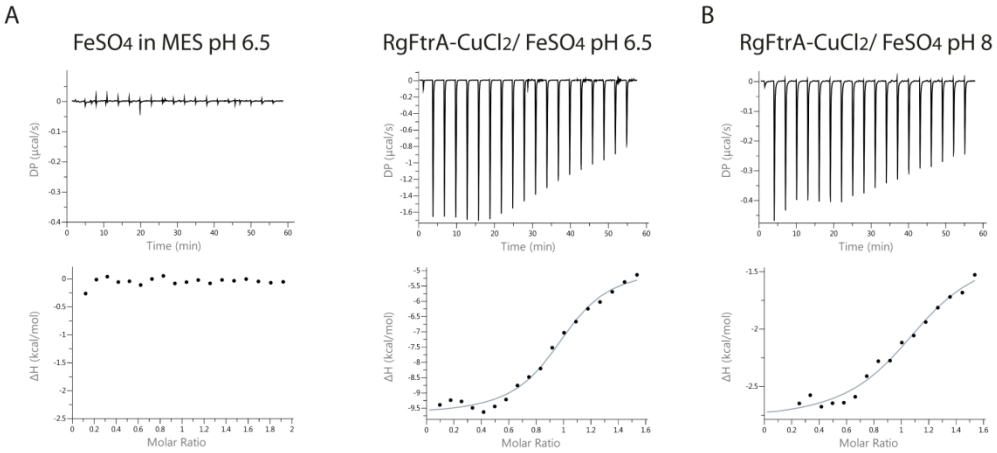
186x117mm (300 x 300 DPI)




| 25°C | n | $K_D$ (µM) | $\Delta H$ (kcal/mol) | $-T\Delta S$ (kcal/mol) | $\Delta G$ (kcal/mol) |
|---|---|---|---|---|---|
| **RgFtrA / $CuCl_2$** | 0.7 | 0.51 | -2.3 | -6.29 | -8.59 |
| **RgFtrA / $ZnSO_4$** | 0.7 | 2.55 | -6.54 | -1.09 | -7.53 |
| **RgFtrA / $NiSO_4$** | 0.7 | 21.9 | -6.42 | -1.27 | -6.36 |

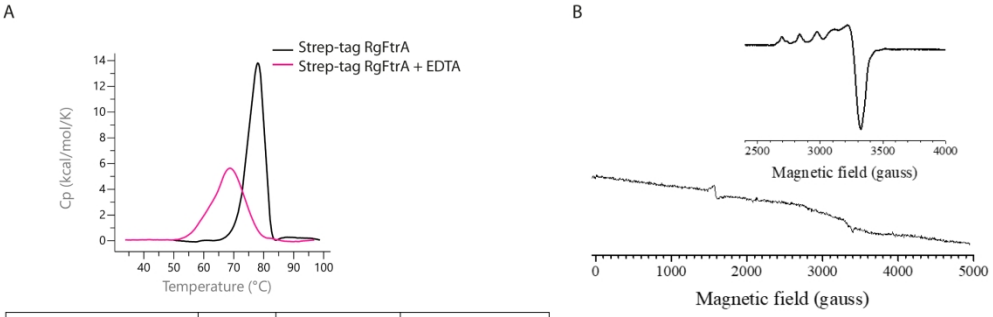
Figure 4

161x119mm (300 x 300 DPI)




| 25°C | n | $K_D$ (µM) | $\Delta H$ (kcal/mol) | $-T\Delta S$ (kcal/mol) | $\Delta G$ (kcal/mol) |
|---|---|---|---|---|---|
| **RgFtrA-$CuCl_2$ / $FeSO_4$ pH 6.5** | 0.97 | 3.33 | -4.82 | -2.66 | 7.48 |
| **RgFtrA-$CuCl_2$ / $FeSO_4$ pH 8** | 1.11 | 5.83 | -1.48 | -5.67 | 7.14 |

Figure 5




| | ***Tm* (°C)** | **$\Delta H_t$ (kcal/mol)** | **$\Delta HVH_t$ (kcal/mol)** |
|---|---|---|---|
| **Strep-tag RgFtrA** | 77.32 | 92.2 | 147 |
| **Strep-tag RgFtrA + EDTA** | 68.18 | 73.3 | 69.8 |

Figure 6

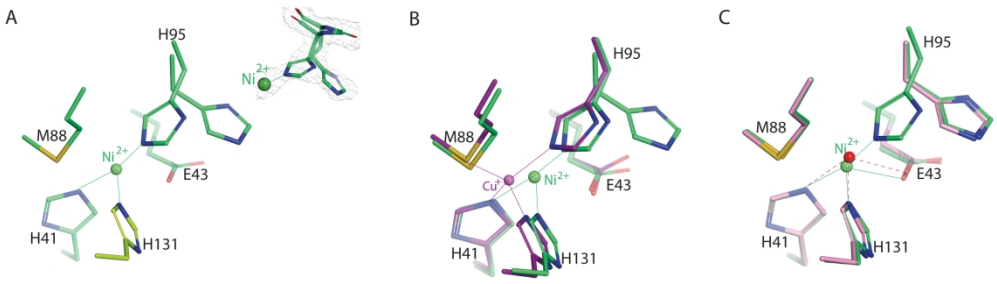



Figure 7

189x54mm (300 x 300 DPI)

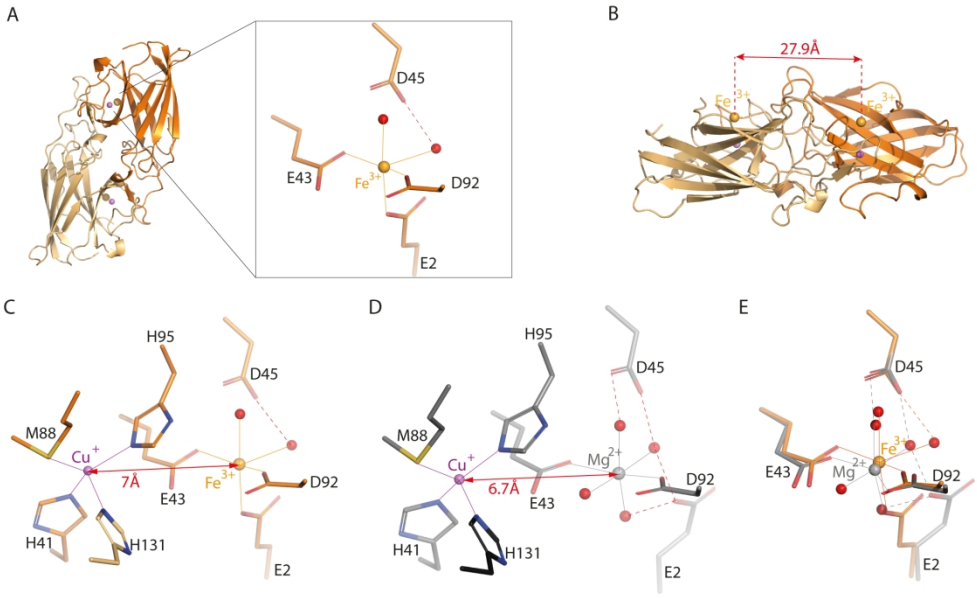



Figure 8

187x113mm (300 x 300 DPI)

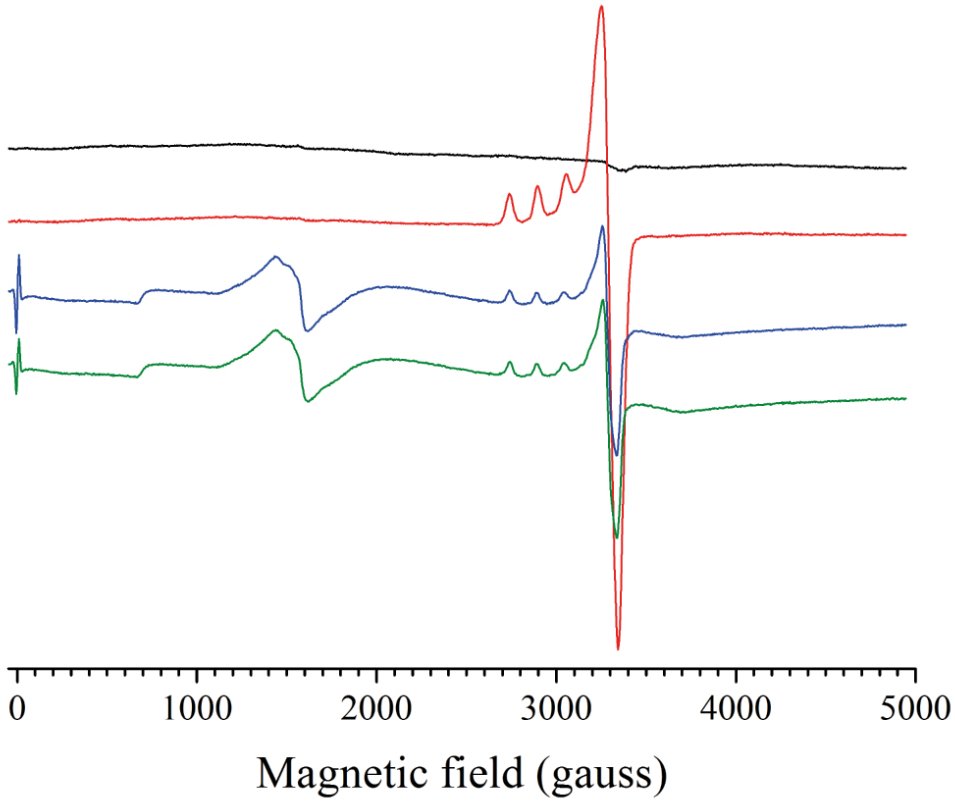
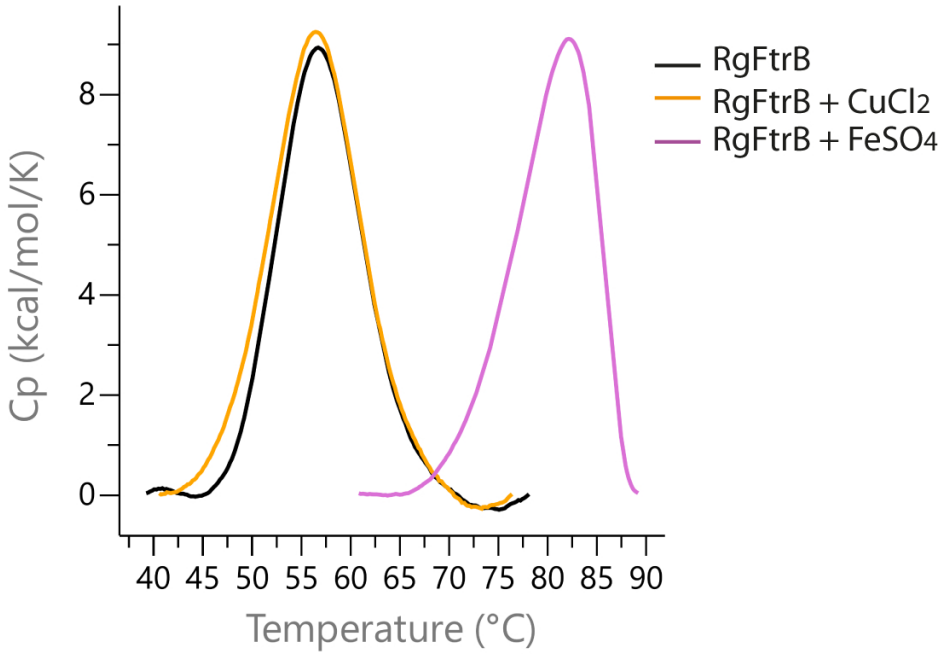



Figure 9

86x72mm (300 x 300 DPI)




| | ***Tm*** **(°C)** | **Δ*Tm*** **(°C)** | **Δ*H*ₗ** **(kcal/mol)** | **Δ*HVH*ₗ** **(kcal/mol)** |
|---|---|---|---|---|
| **RgFtrB** | 56.70 | | 96.6 | 81.5 |
| + $CuCl_2$ | 56.27 | -0.43 | 108 | 74.3 |
| + $FeSO_4$ | 81.01 | 24.32 | 96.1 | 94.9 |

Figure 10

99x102mm (300 x 300 DPI)




Figure 11

100x41mm (300 x 300 DPI)

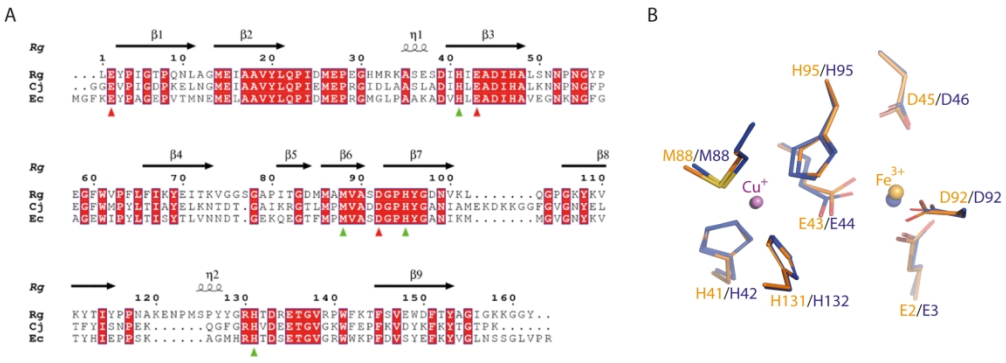

A
B
H95/H95
D45/D46
M88/M88
Cu+
Fe3+
D92/D92
E43/E44
H41/H42
H131/H132
E2/E3

Figure 12

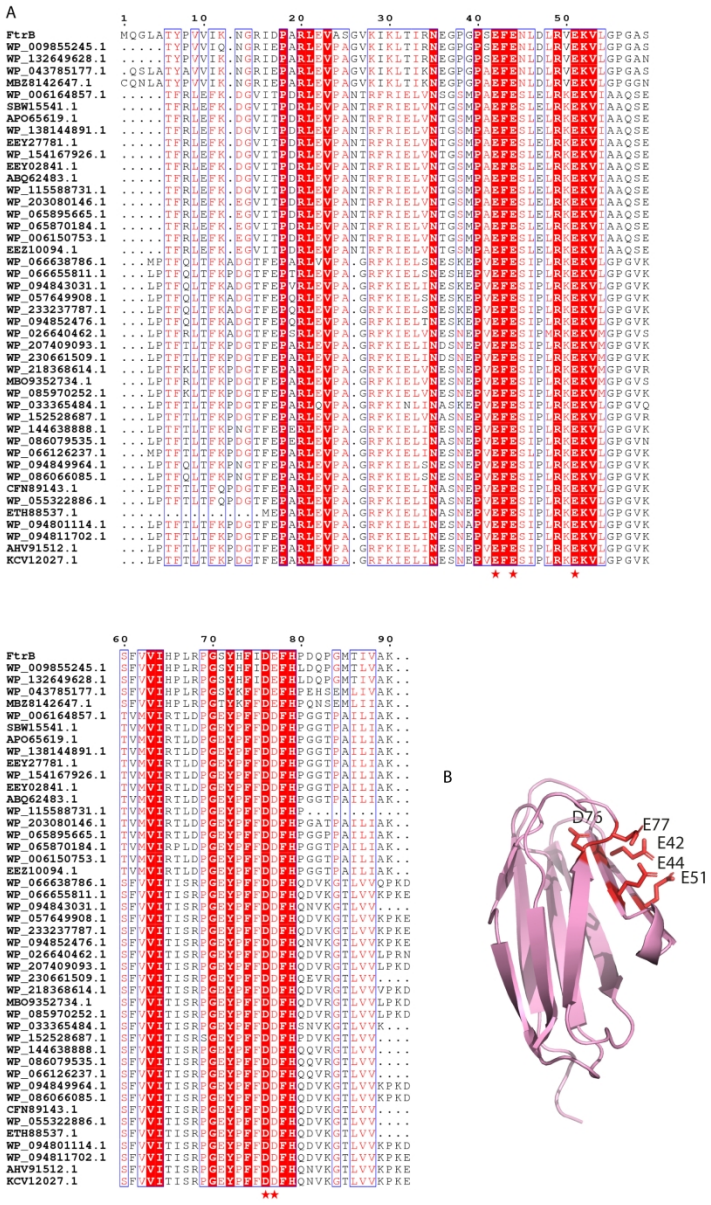



Figure 13

176x289mm (300 x 300 DPI)

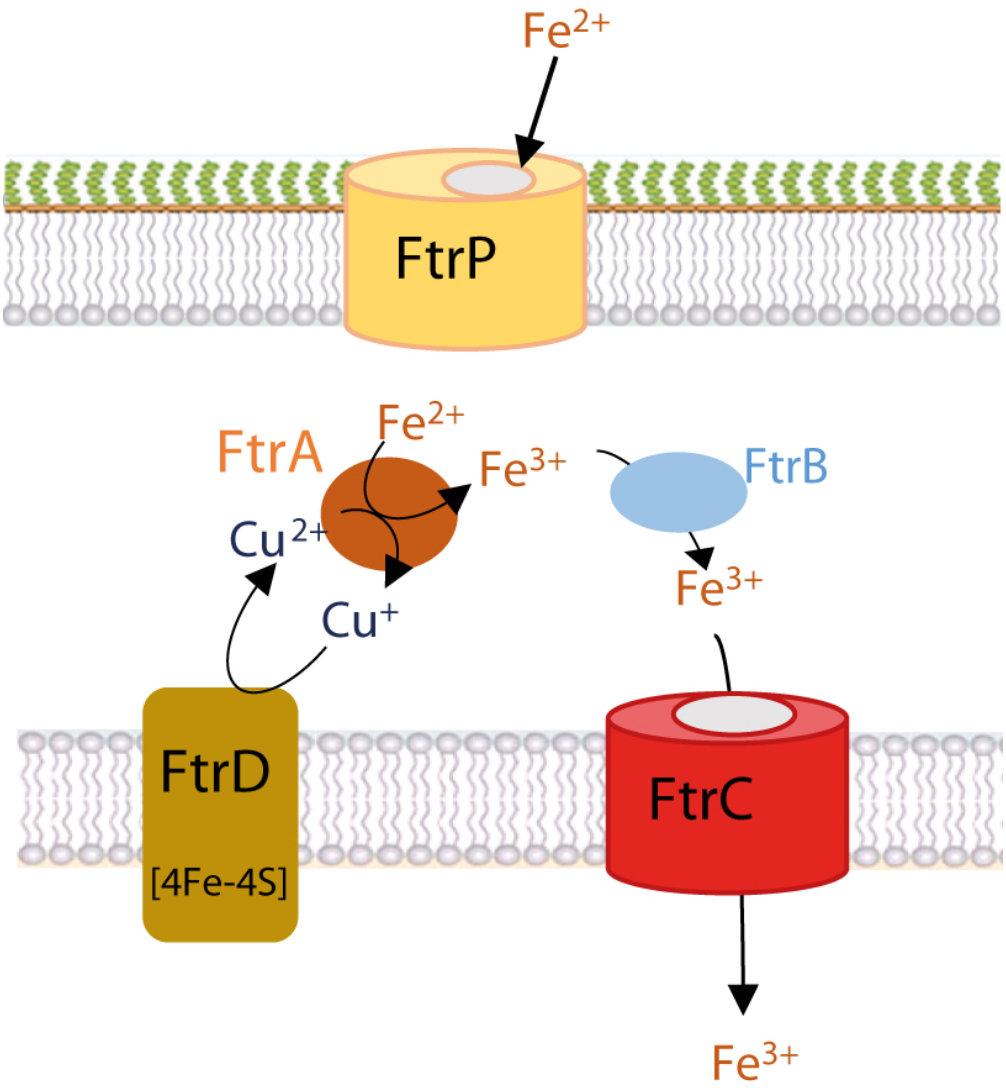



Figure 14

68x76mm (300 x 300 DPI)